Diffraction phase microscopy: principles and applications in materials and life sciences

Basanta Bhaduri,[1] Chris Edwards,[2] Hoa Pham,[1] Renjie Zhou,[2] Tan H. Nguyen,[1] Lynford L. Goddard,[2] and Gabriel Popescu[1,*]

[1]Quantitative Light Imaging Laboratory, Department of Electrical and Computer Engineering, Beckman Institute for Advanced Science and Technology, University of Illinois at Urbana-Champaign, Urbana, Illinois 61801, USA

[2]Micro and Nanotechnology Laboratory, Department of Electrical and Computer Engineering, University of Illinois at Urbana-Champaign, Urbana, Illinois 61801, USA

*Corresponding author: gpopescu@illinois.edu

Received July 9, 2013; revised January 5, 2014; accepted January 27, 2014; published March 26, 2014 (Doc. ID 193585)

The main obstacle in retrieving quantitative phase with high sensitivity is posed by the phase noise due to mechanical vibrations and air fluctuations that typically affect any interferometric system. In this paper, we review diffraction phase microscopy (DPM), which is a common-path quantitative phase imaging (QPI) method that significantly alleviates the noise problem. DPM utilizes a compact Mach–Zehnder interferometer to combine several attributes of current QPI methods. This compact configuration inherently cancels out most mechanisms responsible for noise and is single-shot, meaning that the acquisition speed is limited only by the speed of the camera employed. This technique is also nondestructive and does not require staining or coating of the specimen. This unique collection of features enables the DPM system to accurately monitor the dynamics of various nanoscale phenomena in a wide variety of environments. The DPM system can operate in both transmission and reflection modes in order to accommodate both transparent and opaque samples, respectively. Thus, current applications of DPM include measuring the dynamics of biological samples, semiconductor wet etching and photochemical etching processes, surface wetting and evaporation of water droplets, self-assembly of nanotubes, expansion and deformation of materials, and semiconductor wafer defect detection. Finally, DPM with white light averages out much of the speckle background and also offers potential for spectroscopic measurements.

OCIS codes: (050.1950) Diffraction gratings; (110.0180) Microscopy; (120.3890) Medical optics instrumentation; (120.3940) Metrology; (120.5050) Phase measurement; (110.3175) Interferometric imaging
http://dx.doi.org/10.1364/AOP.6.000057

Diffraction phase microscopy: principles and applications in materials and life sciences

Basanta Bhaduri, Chris Edwards, Hoa Pham, Renjie Zhou, Tan H. Nguyen, Lynford L. Goddard, and Gabriel Popescu

1. Introduction

Ever since the development of phase contrast microscopy in the 1930s by Fritz Zernike, it has been realized that the *phase* of light is an extremely powerful reporter on specimen morphology and topography [1,2]. This principle stems from the knowledge that an ideal imaging system produces an image field that is a scaled replica of the sample field in both amplitude and phase. Thus, phase sensitive measurements at the image plane relate to the local optical properties (refractive index, thickness) of the object under investigation. Phase contrast microscopy made such an important impact in biology that it earned Zernike the Nobel Prize in Physics in 1953.

In 1948, Gabor published his famous paper entitled "A new microscopic principle," in which he proposed the use of optical phase information to correct aberrations in electron micrographs [3]. While the proposed method has never truly solved the aberration issues in electron microscopy, it generated instead a new optical field—*holography*—for which Gabor received the Nobel Prize in Physics in 1971. In essence, Gabor, an electrical engineer with knowledge of communication theory [4], introduced the idea that imaging is a form of transmission of information. Interestingly, the spatial analog to a *carrier frequency* was introduced much later by Lohmann [5] and by Leith and Upatnieks [6]. This approach, known as *off-axis holography*, has a major practical advantage over Gabor's original idea (*in-line holography)* as it can decouple the contributions between the illuminating wave and the field scattered by the object. The first demonstration of the feasibility of the numerical reconstruction of holograms was performed by Goodman and Lawrence [7]. A fast Fourier transform method for analyzing fringes in off-axis holography was reported by Takeda *et al.* in 1982 and became broadly adopted in the field [8]. The impact of digital holography on microscopy became significant much later in the 1990s when implemented with charge-coupled devices (CCDs) as the detector. In 1994 Schnars and Jüptner demonstrated "lensless" off-axis digital holography using a CCD as detector [9]. Soon after, the benefits of digital holography were exploited in microscopy by several groups, in particular, the groups led by Yamaguchi [10], Depeursinge [11], von Bally [12,13], Ferraro [14,15], Kim [16–18], Wax [19–21], Asundi [22,23], Poon [24], and others [25–28].

Interferometry and holography have become invaluable tools in optical metrology, especially because they provide information about material topography with nanoscale accuracy [29]. Since the 1950s, scientists have recognized the potential of optical phase to provide *quantitative* information about

biological specimens, including cell dry mass [30,31]. In the past two decades, quantitative phase imaging (QPI), in which the optical path-length map across a specimen is measured, has become a rapidly emerging field with important applications in biomedicine [32]. QPI utilizes the fact that the phase of a field is much more sensitive to the specimen structure than its amplitude. As fields from the source interact with the specimen, phase shifts are induced in the scattered field with respect to the unscattered light. This phase shift contains the desired structural information about the sample under investigation. Because of the nature of photon absorption, and the limited speed of electronic components, cameras and detectors can measure only intensity. To obtain the phase information, interferometric as well as non-interferometric methods are employed. Recently, a number of such methods have been developed by various groups around the world for quantitatively imaging biological specimens [16–20,33–46].

The main obstacle in retrieving quantitative phase images with high sensitivity is posed by the phase noise due to mechanical vibrations and air fluctuations that typically affect any interferometric system. In this paper, we review diffraction phase microscopy (DPM) [42], which is a common-path QPI method that significantly alleviates the noise problem. DPM utilizes a compact Mach–Zehnder interferometer to combine all of the best attributes of current QPI methods in an efficient and elegant manner. This compact configuration is common-path, which inherently cancels out most mechanisms responsible for noise, and is single-shot, meaning that the acquisition speed is limited only by the speed of the camera employed. This technique is also nondestructive and does not require staining or coating of the specimen. This unique collection of features enables the DPM system to accurately monitor the dynamics of various nanoscale phenomena in a wide variety of environments. The DPM system can operate in both transmission and reflection modes in order to accommodate both transparent and opaque samples. Thus, current applications of DPM include measuring the dynamics of biological samples, semiconductor wet etching and photochemical etching processes, surface wetting and evaporation of water droplets, self-assembly of nanotubes, expansion and deformation of materials, and semiconductor wafer defect detection. Finally, DPM with white light averages out much of the speckle background and also offers potential for spectroscopic measurements.

This review aims at summarizing the principles of the DPM operation, the design constraints, its various experimental implementations and applications in materials and life sciences.

2. Principles of DPM

2.1. Theory

Figure 1 shows a schematic of the DPM system, which can be placed at the output port of any conventional light microscope. The DPM interferometer is created using a diffraction grating in conjunction with a $4f$ lens system. In this geometry, the interferometer is very stable, allowing highly sensitive time-resolved measurements.

Because of the periodic nature of the diffraction grating, multiple copies of the image are created at different angles. Here, we are concerned only with the

Figure 1

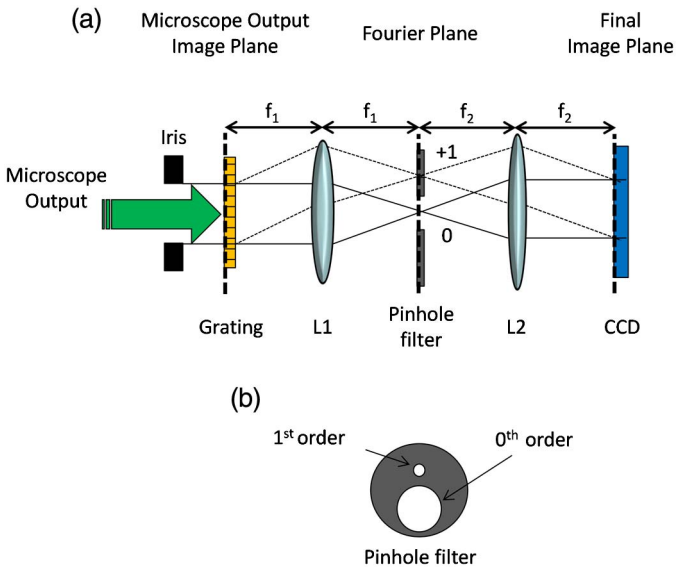

DPM. (a) A diffraction grating is used in conjunction with a $4f$ system in order to produce interference and obtain the phase information from the scattered fields. The grating is placed at the output image plane of the microscope, which creates copies of the image at different angles, some of which are captured by the first lens. Under a $4f$ configuration, the first lens takes a Fourier transform, creating a Fourier plane. (b) A spatial filter is placed in the Fourier plane, which allows the full 0th order to pass, and the 1st order is filtered down using a small pinhole such that after the second lens takes a Fourier transform, the field becomes a uniform plane wave and serves as the reference to the interferometer. The two fields interfere at the final image plane on the CCD sensor to create the interferogram.

0th and +1st orders, which create the final interferogram at the CCD plane. The other orders either do not pass through the first lens or are filtered out in the Fourier plane.

Starting in the grating plane (denoted by the subscript GP) we have

$$U_{\mathrm{GP}}(x,y) = U_0(x,y) + U_1(x,y)e^{i\beta x}, \tag{2.1-1}$$

where U_0 is the 0th order field and U_1 is the +1st order field. Here, $\beta \equiv 2\pi/\Lambda$, where Λ is the grating period. The two fields have the same spatial distribution but may have different amplitudes depending on the grating efficiency. For example, a blazed grating can be used to make the +1st order have much higher amplitude so that, after filtering, the amplitudes are better matched and the fringe visibility on the final interferogram is more optimal.

The first $2f$ system takes a Fourier transform of this field such that before the filter in the Fourier plane (denoted by the subscript FP–) we have

$$\tilde{U}_{\mathrm{FP-}}(k_x,k_y) = \tilde{U}_0(k_x,k_y) + \tilde{U}_1(k_x-\beta,k_y), \tag{2.1-2a}$$

$$k_x = 2\pi x_1/(\lambda f_1) \equiv \alpha x_1, \qquad k_y = 2\pi y_1/(\lambda f_1) \equiv \alpha y_1, \tag{2.1-2b}$$

$$\beta = 2\pi/\Lambda = 2\pi\Delta x/(\lambda f_1) \equiv \alpha\Delta x, \qquad \Delta x = \lambda f_1/\Lambda, \tag{2.1-2c}$$

where (x_1, y_1) are the coordinates at the Fourier plane. Equation (2.1-2b) shows the relationship between the angular spatial frequency variables and their actual location in free space. The quantity Δx represents the physical spacing between the two diffraction orders in the Fourier plane. This value will be re-derived in the next section using simple geometrical optics and used in the design process. From Eq. (2.1-2a), we can see that we have two separate Fourier transforms of the image separated in space.

Because we chose a blazed grating, the 1st order is brighter than the 0th order in the Fourier plane. It is filtered down using a small enough pinhole such that after passing through the second lens this field approaches a plane wave at the camera plane where the transverse amplitude and phase are uniform. This beam serves as our reference for the interferometer. Immediately after the pinhole (denoted by the subscript FP+), we have

$$\begin{aligned}\tilde{U}_{\mathrm{FP}+}(\alpha x_1, \alpha y_1) &= \tilde{U}_0(\alpha x_1, \alpha y_1) + \tilde{U}_1(\alpha x_1 - \beta, \alpha y_1) * \delta(\alpha x_1 - \beta, \alpha y_1) \\ &= \tilde{U}_0(\alpha x_1, \alpha y_1) + \tilde{U}_1(0,0)\delta(\alpha x_1 - \beta, \alpha y_1).\end{aligned} \tag{2.1-3}$$

In Eq. (2.1-3), $\tilde{U}_1(0,0)\delta(\alpha x_1 - \beta, \alpha y_1)$ is the spatial frequency domain representation of the DC signal and $\tilde{U}_0(\alpha x_1, \alpha y_1)$ is the unfiltered signal that contains the image information. So, in the Fourier plane we have one beam carrying all of the information contained in the original image (0th order) and a second beam which carries only the DC content of the original image and serves as our reference beam (1st order).

The second $2f$ system takes another forward Fourier transform, resulting in

$$\begin{aligned}\mathrm{F.T}\{\tilde{U}_{\mathrm{FP}+}(\alpha x_1, \alpha y_1)\} &= \mathrm{F.T}\{\tilde{U}_0(\alpha x_1, \alpha y_1) + \tilde{U}_1(0,0)\delta(\alpha x_1 - \beta, \alpha y_1)\} \\ &= \frac{1}{|\alpha|}(U_0(\xi/\alpha, \eta/\alpha) + \tilde{U}_1(0,0)e^{-i\xi\beta/\alpha}),\end{aligned} \tag{2.1-4a}$$

$$\xi \equiv 2\pi x/\lambda f_2, \qquad \eta \equiv 2\pi y/\lambda f_2. \tag{2.1-4b}$$

At the camera plane (denoted by the subscript CP), the resulting field is

$$U_{\mathrm{CP}}(x,y) = \frac{1}{|\alpha|}[U_0(-x/M_{4f}, -y/M_{4f}) + U_1(0,0)e^{i\beta x/M_{4f}}], \tag{2.1-5a}$$

$$M_{4f} \equiv -f_2/f_1, \tag{2.1-5b}$$

where terms containing α, ξ, and η have been canceled out and the magnification of the $4f$ system, M_{4f}, has been substituted into the equation.

In deriving the irradiance on the CCD camera, we write U_0 and U_1 in phasor form as

$$U_0(x,y) \equiv A_0(x,y)e^{i\phi_0(x,y)}, \qquad U_1(x,y) \equiv A_1(x,y)e^{i\phi_1(x,y)}. \tag{2.1-6}$$

Now, Eq. (2.1-5a) becomes

$$U_{\mathrm{CP}}(x,y) = \frac{1}{|\alpha|}\left(A_0(-x/M_{4f}, -y/M_{4f})e^{i\phi_0(-x/M_{4f},-y/M_{4f})} + A_1(0,0)e^{i\beta x/M_{4f}}e^{i\phi_1(0,0)}\right). \tag{2.1-7}$$

To further simplify, on the right-hand side we change $-x/M_{4f} \to x'$, $-y/M_{4f} \to y'$, $A_0/|\alpha| \to A_0'$, $A_1/|\alpha| \to A_1'$, so

$$U_{\mathrm{CP}}(x,y) = A_0'(x',y')e^{i\phi_0(x',y')} + A_1'e^{-i\beta x'}e^{i\phi_1}. \tag{2.1-8}$$

At the camera plane we have the interference of two magnified copies of the image, where one is filtered to DC, and both are inverted in x and y. The inversion results because two forward transforms are taken by the lenses rather than a transform pair. The resulting intensity measured at the CCD is as follows:

$$\begin{aligned} I_{\mathrm{CP}}(x',y') &= U_{\mathrm{CP}}(x,y)U_{\mathrm{CP}}^*(x,y) \\ &= |A_0'(x',y')|^2 + |A_1'|^2 + 2|A_1'||A_0'(x',y')|\cos(\beta x' + \Delta\phi), \end{aligned} \tag{2.1-9a}$$

$$I_{\mathrm{CP}}(x',y') = I_0(x',y') + I_1 + 2\sqrt{I_0(x',y')I_1}\cos(\beta x' + \Delta\phi), \tag{2.1-9b}$$

$$\Delta\phi = \phi_0(x',y') - \phi_1. \tag{2.1-9c}$$

The phase information from the sample can be extracted from the modulation (cosine) term which is a result of the interference between the image and the reference beam.

2.2. Design Principles

When designing a DPM system, the final transverse resolution of the image is determined by two parameters: the optical resolution of the microscope and the period of the grating, as detailed below.

2.2a. Transverse Resolution

For a microscope operating in transmission mode, with $\mathrm{NA_{obj}}$ and $\mathrm{NA_{con}}$ the objective and condenser numerical apertures, the resolution is given by Abbe's formula [47]:

$$\begin{aligned} \Delta\rho &= \frac{1.22\lambda}{(\mathrm{NA_{obj}} + \mathrm{NA_{con}})} \\ &\simeq \frac{1.22\lambda}{\mathrm{NA_{obj}}}, \end{aligned} \tag{2.2-1}$$

where we assumed plane wave illumination ($\mathrm{NA_{con}} \simeq 0$). The resolution obtained from Abbe's formula is calculated according to the Rayleigh criterion, and the quantity $\Delta\rho$ represents the diffraction spot radius or the distance from the peak to the first zero of the Airy pattern. The resolution of our DPM system ranges from approximately 700 nm (63×, 0.95 NA) to 5 μm (5×, 0.13 NA) depending on the objective being used. To get better resolution at a given wavelength, a higher NA is required. This is typically obtained by using a higher

magnification objective that captures larger angles from the sample plane. A higher NA typically means a higher magnification, which results in a smaller field of view (FOV).

2.2b. Sampling: Grating Period and Pixel Size

The grating is essentially sampling the image. Thus, unless the grating period is sufficiently fine, this sampling degrades the native optical resolution of the microscope. Intuitively, as a result of the Nyquist theorem, we may expect that two periods per diffraction spot give the minimum grating period. It turns out that, due to the interferometric setup, this number must be slightly revised. To understand the frequency coverage of the interferogram, we take the Fourier transform of Eq. (2.1-9a) and obtain

$$\begin{aligned}\tilde{I}_{\mathrm{CP}}(k_x,k_y) &= \mathrm{FT}[I_{\mathrm{CP}}(x',y')]\\ &= \mathrm{FT}[U_0(x',y')U_0^*(x',y') + U_1U_1^* + U_0(x',y')U_1^*e^{i\beta x'}\\ &\quad + U_0^*(x',y')U_1e^{-i\beta x'}]\\ &= \tilde{U}_0(k_x,k_y)\circledcirc\tilde{U}_0^*(-k_x,-k_y) + |U_1|^2\delta(k_x,k_y)\\ &\quad + \tilde{U}_0(k_x,k_y)U_1^*\circledcirc\delta(k_x-\beta,k_y) + \tilde{U}_0^*(-k_x,-k_y)U_1\circledcirc\delta(k_x+\beta,k_y).\end{aligned} \tag{2.2-2}$$

In Eq. (2.2-2), we used the *correlation theorem* for Fourier transformations, i.e., $U_0(x,y)U_0^*(x,y) \to \tilde{U}_0(k_x,k_y)\circledcirc\tilde{U}_0^*(-k_x,-k_y)$; the shift theorem, i.e., $e^{i\beta x'} \to \delta(k_x-\beta,k_y)$, the convolution theorem, i.e., $U_0(x,y)U_1^*e^{i\beta x'} \to \tilde{U}_0(k_x,k_y)U_1\circledcirc\delta(k_x-\beta,k_y)$; and the assumption that U_1 is uniform after passing through the pinhole filter, i.e., $U_1U_1* \to |U_1|^2\delta(k_x,k_y)$; (symbol $\circledcirc$ denotes the *convolution* operation). Note that the convolution of a function with the flipped version of itself, $\tilde{U}_0(k_x,k_y)\circledcirc\tilde{U}_0^*(-k_x,-k_y)$, amounts to an autocorrelation.

Figure 2 shows the Fourier transform of the DPM interferogram represented in the sample plane. Because of interference [Eq. (2.1-9a)], the radius of the central lobe is $2k_0\mathrm{NA}_{\mathrm{obj}}$ and the radius of the sidelobes is $k_0\mathrm{NA}_{\mathrm{obj}}$. To avoid aliasing errors from overlapping frequencies in the Fourier plane, the grating modulation frequency must be chosen such that

$$\beta \geq 3k_0\mathrm{NA}_{\mathrm{obj}}, \tag{2.2-3a}$$

where modulation frequency β (in the sample plane) is defined as $\beta = (2\pi/\Lambda)M_{\mathrm{obj}}$, with Λ the period of the grating and M_{obj} the magnification of the microscope. Thus, from the sampling constraint above, we find that

$$\Lambda \leq \frac{\lambda M_{\mathrm{obj}}}{3\mathrm{NA}_{\mathrm{obj}}}. \tag{2.2-3b}$$

This is the basic criterion and provides an upper bound on the selection of the grating period. Expressing $\mathrm{NA}_{\mathrm{obj}}$ in terms of the diffraction spot size using Eq. (2.2-1), we find

$$\Lambda \leq \frac{\Delta\rho M_{\mathrm{obj}}}{3.66}. \tag{2.2-3c}$$

This states that we need at least 3.66 grating fringes per diffraction spot radius in order to operate at optimal resolution and avoid aliasing.

Figure 2

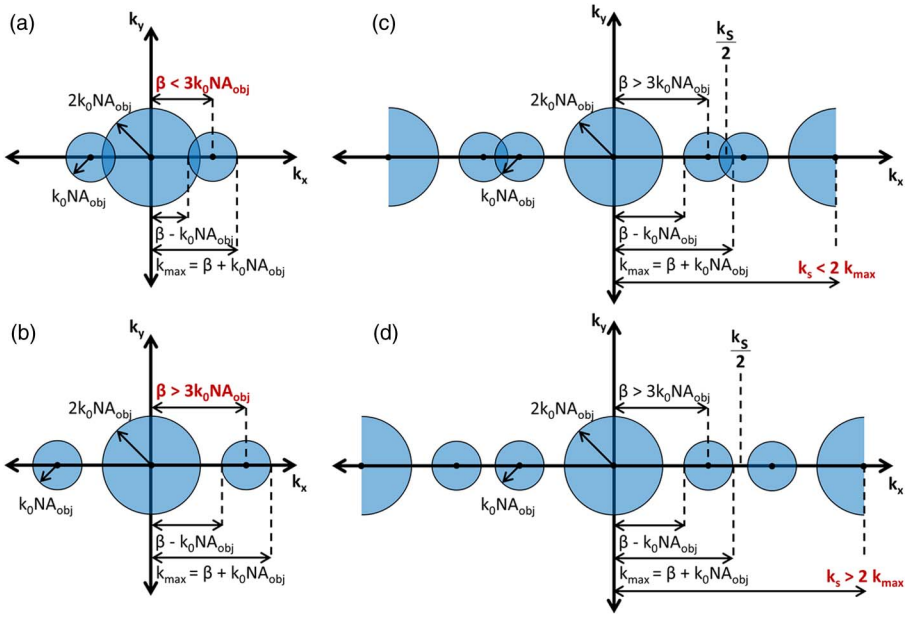

Fourier transform of the intensity at the CCD as represented in the sample plane. Because of interference, the radius of the central lobe is $2k_0\mathrm{NA}_{\mathrm{obj}}$ and the radius of the sidelobes is $k_0\mathrm{NA}_{\mathrm{obj}}$. To avoid aliasing effects and allow for proper reconstruction of the desired signal, the modulation frequency β must be $\geq 3k_0\mathrm{NA}_{\mathrm{obj}}$ and the sampling (pixel) frequency $k_s \geq 2(\beta + k_0\mathrm{NA}_{\mathrm{obj}})$. (a) Aliasing as a result of the grating period being too large. (b) Grating period is small enough to avoid aliasing. (c) Sampling by the CCD pixels does not meet the Nyquist criterion, resulting in aliasing even if the grating period is chosen correctly. (d) The grating period is small enough to push the modulation outside the central lobe and sampling by the CCD pixels satisfies the Nyquist criterion; no aliasing occurs.

To properly sample the interferogram by the CCD pixels, the Nyquist theorem demands that

$$k_s \geq 2k_{\max} = 2(\beta + k_0\mathrm{NA}_{\mathrm{obj}}), \tag{2.2-4}$$

where k_s is the pixel sampling frequency, and M_{4f} is the magnification of the $4f$ system that images the grating at the CCD plane. This magnification can be used as a tuning knob for the system as it can adjust the grating period relative to the pixel size at the CCD plane. If we denote the physical pixel size of the camera as a, the constraint necessary to avoid aliasing due to pixel sampling is

$$k_s = \frac{2\pi}{a} M_{\mathrm{obj}} |M_{4f}| \geq 2(\beta + k_0\mathrm{NA}_{\mathrm{obj}}), \tag{2.2-5a}$$

which leads to

$$|M_{4f}| \geq 2a\left[\frac{1}{\Lambda} + \frac{1}{\lambda}\frac{\mathrm{NA}_{\mathrm{obj}}}{M_{\mathrm{obj}}}\right]. \tag{2.2-5b}$$

This is another important criterion stating the minimum $4f$ magnification for a given grating period. Note that if Eq. (2.2-3b) holds and if

$$|M_{4f}| \geq \frac{8a}{3\Lambda}, \tag{2.2-5c}$$

then the Nyquist sampling condition will be satisfied. This simply states that having at least 2.67 pixels per fringe is a sufficient condition. Although this provides an approximate lower bound on the $4f$ magnification, a slightly smaller $4f$ magnification can be chosen according to Eq. (2.2-5b).

2.2c. Field of View (Lens Selection in 4f Configuration)

The $4f$ magnification also dictates the FOV. The FOV (in the sample plane) for an $m \times n$ image can be calculated as follows:

$$\text{FOV} = [m, n]\frac{a}{M_{\text{obj}}|M_{4f}|}. \tag{2.2-6}$$

The image has n rows that represent the y component (up and down) and m columns that represent the x component (left and right).

2.2d. Fourier Plane Spacing (Filter Construction)

The grating period also affects the physical spacing in the Fourier plane, which must be calculated in order to design and build the physical filter. The basic grating equation for the mth diffraction order at normal incidence is

$$\sin\theta_m = m\frac{\lambda}{\Lambda}. \tag{2.2-7a}$$

The distance from the grating to the lens is f_1 and the separation Δx of the 0th and 1st orders after passing through L1 remain nearly constant. Using simple geometry,

$$\tan\theta_m = \frac{\Delta x}{f_1}. \tag{2.2-7b}$$

For small angles, which is a good approximation for our system,

$$\tan\theta_m \approx \sin\theta_m \approx \theta_m. \tag{2.2-7c}$$

Combining with Eq. (2.2-7a) yields the following:

$$\Delta x = \frac{f_1\lambda}{\Lambda}. \tag{2.2-8}$$

This is the same as Eq. (2.1-2c) and is used to design the physical pinhole filter. This distance Δx should be small enough compared to f_1 to fit at least the 0th and 1st orders through the first lens (L1) with the 0th order passing through the center of the lens. This condition is satisfied when the following condition holds:

$$\text{NA}_1 \geq \frac{\lambda}{\Lambda} + \frac{\text{NA}_{\text{obj}}}{M_{\text{obj}}}. \tag{2.2-9}$$

In Eq. (2.2-9), the first term on the right-hand side is due to the physical spacing (Δx) and the second term to the scattered light collected by the objective.

2.2e. Pinhole Size (Uniform Reference at CCD Plane)

The physical low-pass filter can be created by using a small manufactured pinhole for the reference and a larger cutout for the 0th order. The size of the pinhole should be chosen so that the resulting diffraction pattern is nearly uniform over the entire FOV of the CCD. The Fraunhofer diffraction pattern resulting from a plane wave passing through the pinhole filter (circular aperture) of diameter D after L2 performs a Fourier transform is of the form

$$I(x,y) = I_0\left[\frac{2J_1(\pi D\rho/\lambda f_2)}{\pi D\rho/\lambda f_2}\right]^2, \tag{2.2-10}$$

where J_1 is a Bessel function of the first kind, I_0 is the peak intensity, $\rho = \sqrt{x^2+y^2}$, λ is the mean wavelength of the illumination, and f_2 is the focal length of lens L2 [48].

Equating the argument of the jinc function to the location of the first zero allows us to solve for the radius ρ of the central lobe:

$$\frac{\pi D\rho}{\lambda f_2} = 3.83, \tag{2.2-11a}$$

$$\rho = 3.83\frac{\lambda f_2}{\pi D} = 1.22\frac{\lambda f_2}{D}. \tag{2.2-11b}$$

This is a re-derivation of Abbe's formula. As a rule of thumb, the diameter of the central lobe of the jinc function should be much larger, say, by a factor γ, than the diagonal dimension of the CCD sensor so that the reference signal is uniform across the image. We will let $\gamma = 4$ represent this factor. The CCD typically has square pixels but a rectangular sensor, so the diagonal distance "d" should be used in this calculation:

$$d = a\sqrt{m^2+n^2}, \tag{2.2-12a}$$

$$\rho = \frac{1.22\lambda f_2}{D} \geq \frac{\gamma d}{2}, \tag{2.2-12b}$$

$$D \leq \frac{2.44\lambda f_2}{\gamma d}. \tag{2.2-12c}$$

Using a smaller pinhole will make the reference more uniform but will reduce the intensity in the reference beam. This will degrade the fringe visibility. Using a blazed grating as mentioned above helps to better match the intensities, but in general, the pinhole should be just small enough to get a uniform reference beam at the camera plane while keeping as much intensity as possible.

Also, the second lens should be such that both the 0th order and the filtered 1st order fit completely through the second lens. This condition is satisfied when the following condition holds:

$$\mathrm{NA}_{L_2} \geq \frac{\lambda}{|M_{4f}|\Lambda} + \frac{1.22\lambda}{D}. \tag{2.2-13}$$

Although completely passing both orders is ideal, it is not necessary. The two orders need only to overlap in the camera plane to cover the FOV. Assuming Eq. (2.2-12c) holds, a less stringent condition to satisfy this is

$$\mathrm{NA}_{L_2} \geq \frac{\lambda}{|M_{4f}|\Lambda} + \frac{1.22\lambda}{\gamma D}. \tag{2.2-14}$$

Finally, an important figure of merit is the ratio of the unscattered and scattered light beam radii in the Fourier plane. This indicates the degree of coupling between the two components, which should ideally be minimal in order to allow for proper quantitative reconstruction of the phase image. The ratio can be best expressed as follows:

$$\eta = \frac{1.22\lambda M_{\mathrm{obj}}|M_{4f}|}{a\sqrt{m^2+n^2}\mathrm{NA}_{\mathrm{obj}}}. \tag{2.2-15}$$

In the sample plane, this can equivalently be expressed as the ratio of the diffraction spot radius to the FOV diagonal diameter:

$$\eta = \frac{\Delta\rho}{\mathrm{FOV}_{\mathrm{diagonal}}}. \tag{2.2-16}$$

A ratio of 1 means that the diffraction spot is the same size as the FOV and only the DC signal can be obtained. As the ratio approaches zero, more and more detail can be observed within the image for a given FOV.

The design equations for the DPM imaging system are summarized in Table 1.

For a given microscope objective and CCD pixel size, a correct combination of diffraction grating, $4f$ lenses, and pinhole filter must be chosen. The simple rules are that there should be at least 2.67 pixels per fringe and 3.6 fringes per diffraction spot radius. First, the grating period is chosen based on the objective. The magnification of the $4f$ lenses is determined by the grating period and pixel size of the camera. It determines the FOV. The numerical aperture of the first lens, L1, must be chosen so that the two orders used in imaging fit through the lens without obstruction and with the 0th order passing through the center. The physical pinhole used to filter and obtain the reference beam should be chosen such that the resulting diffraction pattern has a large enough central lobe at the camera plane to

Table 1. DPM Design Equations

Equation	Description
$\Delta\rho = \frac{1.22\lambda}{\mathrm{NA}_{\mathrm{obj}}}$	Resolution (diffraction spot radius)
$\Lambda \leq \frac{\lambda M_{\mathrm{obj}}}{3\mathrm{NA}_{\mathrm{obj}}}$	Maximum grating period (separated orders)
$\lvert M_{4f}\rvert \geq 2a\left[\frac{1}{\Lambda} + \frac{1}{\lambda}\frac{\mathrm{NA}_{\mathrm{obj}}}{M_{\mathrm{obj}}}\right]$	Minimum $4f$ magnification (sampling)
$M_{4f} = \frac{-f_2}{f_1}$, $M = M_{\mathrm{obj}}M_{4f}$	Magnification
$\mathrm{FOV} = [m,n]\frac{a}{M_{\mathrm{obj}}\lvert M_{4f}\rvert}$	Resulting FOV in sample plane
$\Delta x = \frac{f_1\lambda}{\Lambda}$	Fourier plane spacing (filter design)
$\mathrm{NA}_{L_1} \geq \frac{\lambda}{\Lambda} + \frac{\mathrm{NA}_{\mathrm{obj}}}{M_{\mathrm{obj}}}$	Minimum NA for lens 1 (avoid clipping)
$D \leq \frac{2.44\lambda f_2}{\gamma d}$	Maximum pinhole diameter (uniform reference beam)
$\mathrm{NA}_{L_2} \geq \frac{\lambda}{\lvert M_{4f}\rvert\Lambda} + \frac{1.22\lambda}{D}$	Minimum NA for lens 2 (avoid clipping)
$\eta = \frac{1.22\lambda M_{\mathrm{obj}}\lvert M_{4f}\rvert}{\mathrm{NA}_{\mathrm{obj}}d} = \frac{\Delta\rho}{\mathrm{FOV}_{\mathrm{diagonal}}}$	Coupling ratio (ratio of DC to AC)

ensure a uniform reference image. Finally, the numerical aperture of the second lens, L2, needs to be large enough for the lens to capture both beams.

2.3. Phase Reconstruction

Before imaging a sample, we first collect a calibration image of a flat featureless region on the sample. This calibration image is used to subtract the background from the image [49,50]. A new calibration image should be taken each time a new sample is measured. If it is not possible to collect a calibration image, then the curvature should be removed using a surface fitting function, although this approach does not remove the background noise.

To illustrate the postprocessing procedure, we imaged one of our samples used for calibration in the Axio Imager Z2 (Zeiss) system. Figure 3 shows raw images of this sample taken directly from the CCD. A 10× objective was used resulting in a 125 μm × 170 μm FOV. Our calibration samples for the epi-DPM system are GaAs micropillars of varying diameters and heights. This particular micropillar is 75 μm in diameter and 110 nm in height. These calibration samples will be discussed in more detail in the next section. Figure 3(a) was taken from a flat featureless portion of the sample. Figure 3(b) shows the raw image of a micropillar. The grating period in the sample plane is 333 nm, resulting in roughly 500 fringes across the FOV. The small period of the fringes makes them difficult to see with the naked eye. Multiple scratches from the grating can be seen

Figure 3

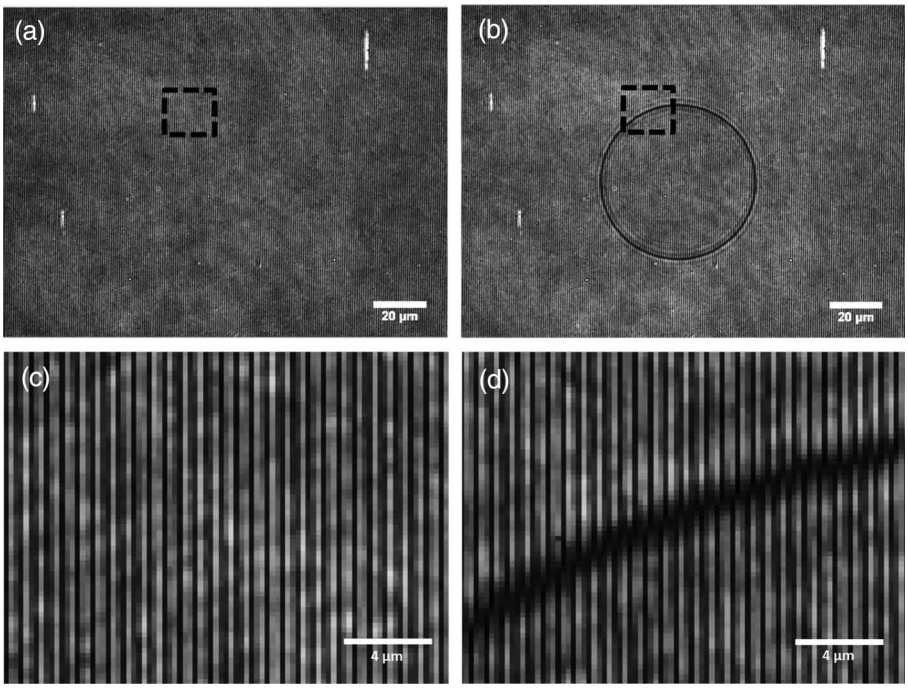

Raw images. (a) Calibration/background image taken from a flat featureless portion of the sample. (b) Image of micropillar (control sample). (c) Zoomed-in portion of the calibration image in (a), showing no shift in the fringes. (d) Zoomed-in portion of the micropillar's edge, showing a horizontal shift in the fringes due to a change in height. The shift of the fringes is proportional to the change in the optical path length.

in identical locations in both the calibration image and the test image. Because the grating is in a conjugate image plane, these scratches show up focused in the raw images. These will not appear in the final phase image after the background is subtracted.

Figure 4(a) shows the Fourier transform of the raw image. A simple bandpass filter centered at $k_x = \beta$ can be used to extract the modulated signal [Fig. 4(b)]. Note that the bandpass filter size is set to $k_0 \mathrm{NA}_{\mathrm{obj}}$ (in the sample plane) to minimize noise without adding any additional low-pass filtering. The filtered

Figure 4

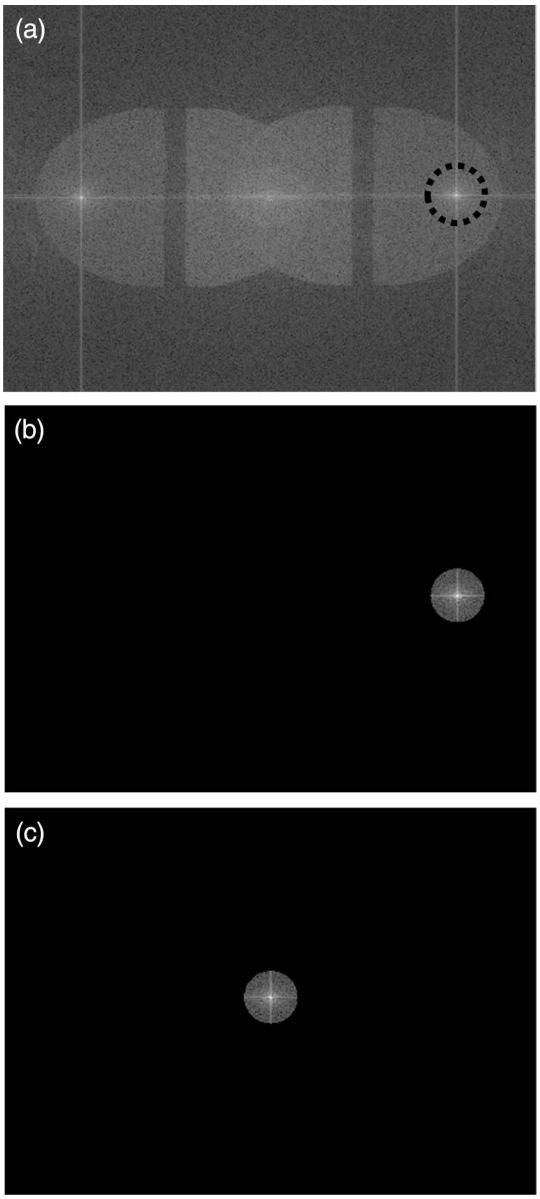

Phase reconstruction. (a) Fourier Transform of raw interferogram. (b) A simple bandpass filter is used to pick out the spatially modulated signal. (c) The signal is brought back to baseband. From here, the phase can be extracted and used to reconstruct the surface profile.

modulated signal is then brought back to baseband [Fig. 4(c)]. This is done separately for both the calibration image and the image of interest.

The background subtraction is then done by dividing the image complex field by its calibration image complex field [49,50]. This approach removes much of the background noise and any tilt in the image associated with the off-axis approach [49]. If necessary, phase unwrapping is then performed using the Goldstein algorithm in order to give proper phase values. The Goldstein algorithm is a good compromise of accuracy and processing time. The height is then calculated in the following manner:

$$h(x,y) = \frac{\varphi(x,y)\lambda_0}{2\pi\Delta n}. \tag{2.3-1}$$

Equation (2.3-1) is valid for transmission. In reflection, however, the light travels to the surface and back requiring an additional factor of 2 to account for the double pass (i.e., replace h by $2h$).

Once the image is leveled and converted to height, the mean (or mode) value of the background is calculated and subtracted from the image so that the background of the image is set to a height of zero. This can also be done using the curve fitting function but with less user control. Figure 5 shows the final phase image, cross-sectional profile, and topographical reconstruction. Notice that the scratches from the grating emphasized in Fig. 3 are no longer present and the background is very clean.

A standard digital bandpass filter (BPF) has abrupt edges and results in a windowing effect, which can be seen in the image shown in Fig. 5. Notice the concentric circles just outside the pillar and in various portions of the background. By using an apodized filter, which is a basic digital BPF with Gaussian edges, the windowing effect can be minimized. To get optimum results, the radius of the ideal LPF should be decreased until right before the quantitative values begin to change. The width of the Gaussian edge is then chosen so that it decays almost

Figure 5

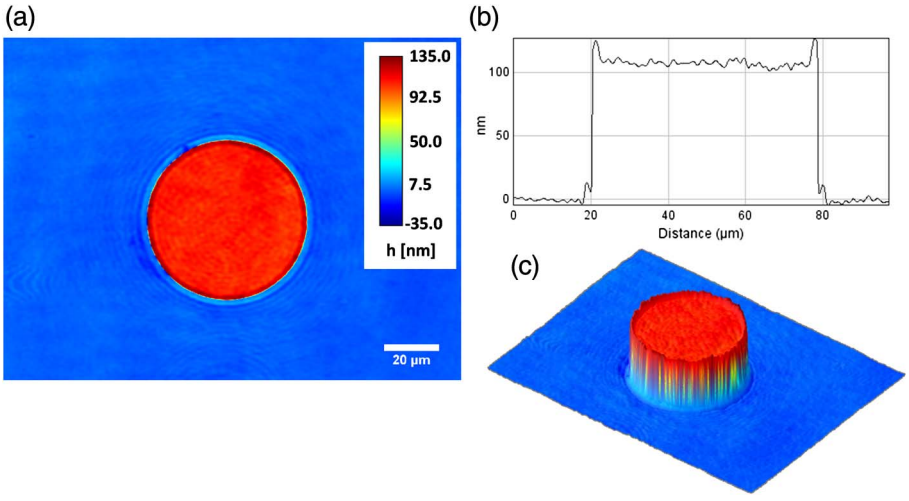

Quantitative phase images obtained via DPM. (a) Height map obtained via DPM. (b) Cross section of the micropillar showing height and diameter. (c) Topographic reconstruction of micropillar in (a).

Figure 6

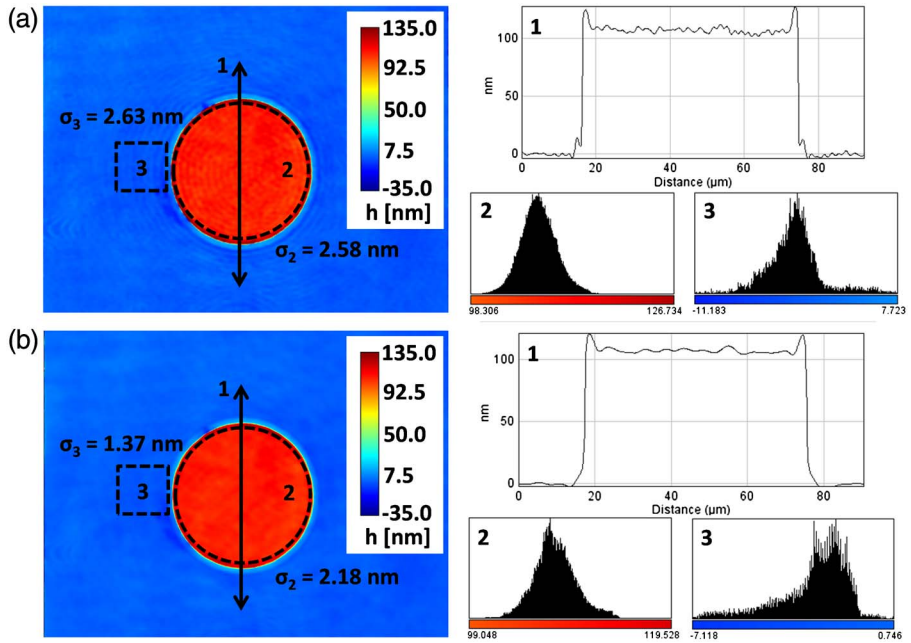

Comparison between standard digital BPF and apodized BPF. (a) Phase image processed using standard digital BPF. (b) Phase image processed using optimized hybrid filter. For both sets of images, region 1 is a cross-sectional profile of the micropillar taken along the vertical line indicated in the DPM image. Region 2 indicates the noise and roughness on top of the pillar, and region 3 indicates the background region near the edge of the micropillar where ringing is most prominent. Notice a clear reduction in the ringing and noise while maintaining the quantitative values. This is not possible using an abrupt BPF or a Gaussian alone; a combination must be employed.

to zero at the edge of the diffraction spot in the Fourier domain ($k_0\mathrm{NA}_{\mathrm{obj}}$ circle), thus eliminating any abrupt cutoff and maintaining correct quantitative values. Figure 6(a) shows the micropillar image from Fig. 5, which uses an abrupt BPF. Figure 6(b) shows the improved image created using an optimized hybrid filter. The reduction in noise and ringing is apparent. A 50% reduction in the spatial noise around the edges of the pillar is seen in histogram 3 by looking at the standard deviation. Note that the height is still correct within a fraction of a nanometer and the width does not change. This is not possible using a Gaussian filter alone; a combination must be employed. Note that there is an extensive array of optimized filters (Hann, Hamming, Bartlett, etc.) for such cases, but we find that our hybrid filter is the simplest to use and still gives the desired improvements.

2.4. System Testing and Noise Characterization

To characterize both the spatial and temporal noise of the system, we imaged a plain, unprocessed n^+GaAs wafer. Two sets of 256 images were acquired at 8.93 frames/s, each from a different FOV approximately 0.5 mm apart. This ensures that the two sequences were not spatially correlated. We used a $10\times$ objective (NA $= 0.25$), which provides a lateral resolution of 2.6 μm and results in a FOV of approximately 160 μm $\times$ 120 μm. One time lapse (set of 256

images) was averaged to obtain a calibration image. The other 256 images were then processed individually using this calibration image. Figure 7(a) shows the height map of a flat, unprocessed n^+GaAs wafer. Ideally, the measured heights should be zero, but of course they are not, due to noise. The root-mean-square (RMS) standard deviation of a single frame was taken in order to quantify the spatial noise. Our spatial noise floor is 2.8 nm. This value represents the variation over the FOV resulting not from any structure, but due to noise itself. The roughness of a typical wafer is about 0.3 nm. Figure 7(b) shows the standard deviation of each individual frame projected over the entire sequence of 256 images. This image shows the standard deviation at each pixel over the entire sequence, which represents our temporal noise. The temporal noise of our system was measured to be 0.6 nm. The subnanometer temporal stability is in large part due to the common path interference method employed.

To verify the proper operation of the DPM imaging system, control samples were fabricated via wet etching of n^+GaAs wafers. The control samples consisted of micropillars etched to specific heights with varying diameters. Photolithography and developing were done using a standard SPR 511A photoresist

Figure 7

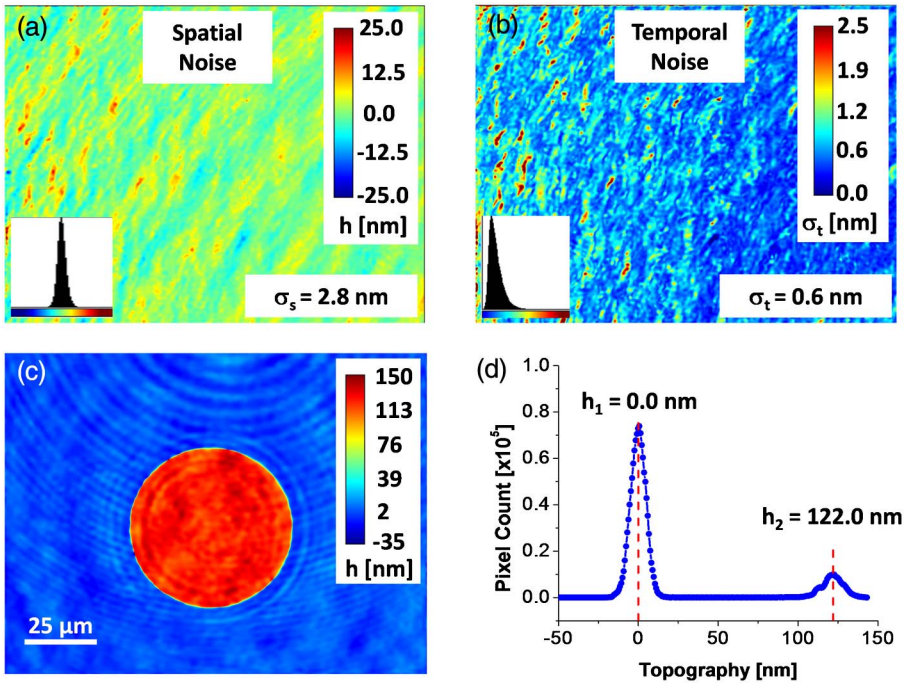

Noise characterization and system verification. (a) Height image of plain unprocessed n^+GaAs wafer. The heights should ideally be zero in all locations. Thus, the standard deviation of the height is a measure of the spatial noise. (b) Images of the standard deviation of each pixel projected over the entire 256 frame sequence. This gives the standard deviation of each pixel over time, which is a measure of the temporal noise in the system. (c) Height map of our micropillar control sample. (d) Histogram of (a) used to extract pillar height. All measured dimensions were verified using the Tencor Alpha-Step 200 surface profiler and the Hitachi S-4800 scanning electron microscope. All measured heights were accurate to within the spatial noise floor, and all lateral dimensions were accurate to within the diffraction spot. Adapted from [50].

recipe. Figures 7(c) and 7(d) show the epi-DPM image and resulting histogram. The height of the pillar with respect to the etched region was extracted from the histogram. The mean height was measured to be 122.0 ± 0.1 nm. All measured dimensions were verified using the Tencor Alpha-Step 200 surface profiler and the Hitachi S-4800 scanning electron microscope. All measured heights were accurate to within the spatial noise floor and all lateral dimensions were accurate to within the diffraction spot. A small degree of nonuniformity among the micropillar heights was observed throughout the sample, which is typical of the wet etching process.

2.5. Derivative Method for Phase Reconstruction

Integral operators (Fourier and Hilbert transforms) are established methods for phase reconstruction in off-axis QPI methods [8,41]. However, because they are integral transformations, these operations are computationally demanding, making it difficult to achieve fast phase extraction. This challenge has been addressed recently by parallelizing the numerical reconstruction [51]. Recently, we presented a *derivative method* for phase reconstructions, which can be applied quite generally to any off-axis interferogram, including DPM [52]. Our *local* method relies on the first- and second-order derivatives of the recorded image and, thus, is 4 times faster than the Hilbert transform technique and 10 times faster than the Fourier transform technique for phase extraction. Further, our approach works with fringes sampled by an arbitrary pixel number, N, as long as $N \geq 8/3$ to satisfy the Nyquist condition for an interferogram (see, e.g., pp. 308 in [32]).

In DPM, the interference pattern can be rewritten as

$$I(x,y) = I_b(x,y) + \gamma(x,y)\cos[\phi(x,y) + \beta x], \tag{2.5-1}$$

where I_b is the background intensity, γ is the modulation factor, ϕ is the phase delay due to the specimen, and β is the spatial frequency of the carrier fringes. The latter is determined by the tilt angle, θ, between the sample and reference beams, that is,

$$\beta = 2\pi \sin\theta/\lambda, \tag{2.5-2}$$

where λ is the wavelength. Typically, the phase is obtained via a spatial Hilbert transform, which provides the complex analytic signal associated with the real interferogram [41,53]. Here we show that, for phase objects, ϕ can be obtained more directly via transverse derivatives of the interferogram. Thus, the first-order derivative of Eq. (2.5-1) with respect to x can be written as

$$\frac{\partial I(x,y)}{\partial x} = \frac{\partial I_b(x,y)}{\partial x} + \cos[\phi(x,y) + \beta x]\frac{\partial \gamma(x,y)}{\partial x} - \gamma(x,y)\sin[\phi(x,y) + \beta x]\left[\frac{\partial \phi(x,y)}{\partial x} + \beta\right]. \tag{2.5-3}$$

For most transparent specimens of interest, i.e., *phase objects*, we can make the following helpful approximations:

$$\frac{\partial I_b}{\partial x} \approx 0, \qquad \frac{\partial \gamma}{\partial x} \approx 0, \qquad \frac{\partial \phi}{\partial x} \ll \beta, \tag{2.5-4}$$

where we consider that the background intensity, I_b, and modulation factor, γ, are constant over the interferogram, and the phase, ϕ, is a slowly varying function. The first two conditions are clearly fulfilled for phase objects, where no intensity modulation is observed. The third assumption, $\partial\phi/\partial x \ll \beta$, applies because we always adjust the fringe period to be smaller than the diffraction spot of the imaging system, such that the optical resolution is not degraded by sampling [41]. Under these circumstances, over a diffraction spot (or central portion of the point spread function), the phase of the field, $\phi(x,y)$, varies *insignificantly*, but the phase of the fringe, βx, changes by at least 2π. Therefore, from Eq. (2.5-3) we have

$$I' = -\frac{\partial I(x,y)}{\partial x} = \gamma\beta \sin[\phi(x,y) + \beta x]. \tag{2.5-5}$$

Similarly, the derivative of Eq. (2.5-5) with respect to x gives the second-order derivative:

$$I'' = -\frac{\partial^2 I(x,y)}{\partial x^2} = \gamma\beta^2 \cos[\phi(x,y) + \beta x]. \tag{2.5-6}$$

Using Eqs. (2.5-5) and (2.5-6), we obtain the phase directly as the argument of the complex function $I'' + ikI'$, with $i = \sqrt{-1}$:

$$\phi(x,y) = \arg(I'' + ikI') - \beta x. \tag{2.5-7}$$

Clearly, this derivative method, based on local operations, is faster than the traditional integral operations. The spatial frequency, β, has fixed value over time and throughout the FOV and is determined by the period of the grating. Thus one needs to measure it only once for a particular experimental system. One of the best options to measure β is by detecting the peak position of one of the first orders in the Fourier transform of the interferogram.

We illustrate the phase reconstruction procedure in Fig. 8. The interferogram (512×512 pixels) associated with a red blood cell (RBC) specimen [Fig. 8(a)] has a spatial frequency, $\beta = 1.83$ rad/pixel. The numerically calculated first and second derivatives of the interferogram are shown in Figs. 8(b) and 8(c), respectively. Since we know β, we can calculate the phase from the two derivative images and remove the tilt due to the carrier fringes [last term in Eq. (2.5-7)]. In calculating the derivatives and the phase, we used MATLAB, but, of course, our method can be implemented with any computing platform.

Figure 8(d) shows the reconstructed phase after 2D phase unwrapping and 3×3 average filtering. The color bar indicates the phase in radians. Some pixel noise is visible because the derivative calculations act as high-pass filters and may introduce high-frequency noise in the image. Fortunately, our images are oversampled to preserve optical resolution (as explained earlier), and it is expected that below the optical resolution, noise is dominant. Therefore, filtering is permissible over an area up to the diffraction spot size, i.e., at least 3 pixels. Further, we have compared this result given by our method with that given by the Hilbert transform [41] [Fig. 8(e)] and obtained excellent agreement. Standard deviation of the difference of phases between Figs. 8(d) and 8(e) is only 0.02 rad, which represents 1.56% of the maximum phase value. We compared the execution time for the phase calculation in both the cases: the Hilbert transform method takes

Figure 8

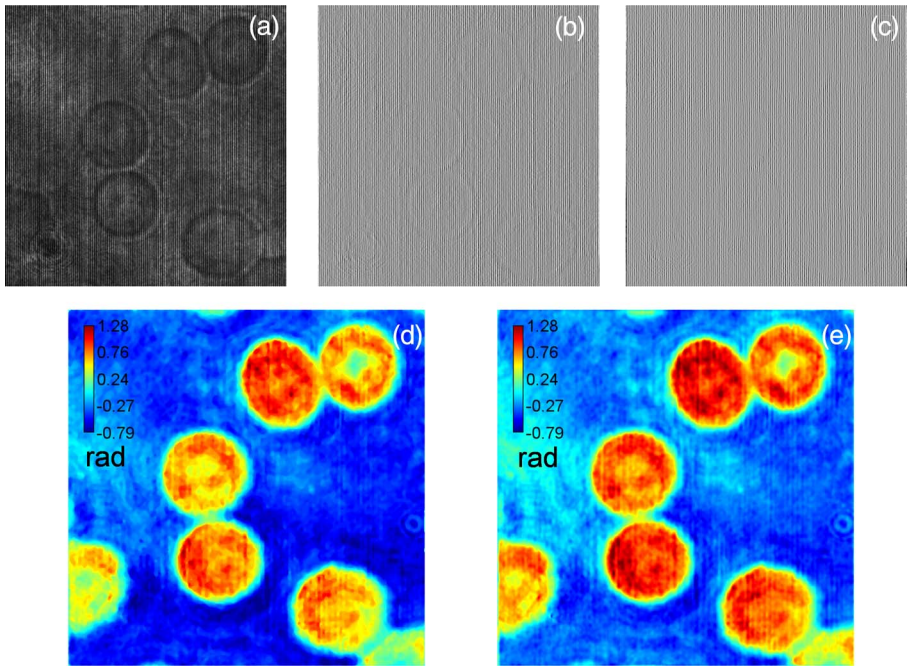

Derivative method for phase calculation. (a) Original DPM image. (b) First-order derivative of (a) with respect to x. (c) Second-order derivative of (a) with respect to x. (d) The reconstructed unwrapped phase. (e) Phase obtained by Hilbert transform; the color bars show the phase in radians.

89.9 ms whereas our derivative method takes only 21.7 ms, which is more than 4 times faster. The phase extraction was performed on a desktop computer (Intel Core i7-960 CPU, 3.20 GHz) in a MATLAB environment.

3. Laser DPM

3.1. Transmission Mode

3.1a. Setup

Figure 9 shows a schematic of the laser DPM system operating in transmission mode. A 532 nm frequency-doubled Nd:YAG laser is used as the source. The source is coupled into a single-mode fiber (SM fiber) and collimated to ensure full spatial coherence. This beam is aligned to the input port of the microscope. The collimated beam passes through the collector lens and is focused at the condenser diaphragm, which is left open. The condenser lens creates a collimated beam in the sample plane. Both the scattered and unscattered fields are captured by the objective lens and focused on its back focal plane. A beam splitter then redirects the light through a tube lens, creating a collimated beam containing the image at the output image plane of the microscope. This is where a camera is typically placed in order to get intensity images, but in DPM we require phase images, so some type of interference must be performed. A diffraction grating is placed at the output image plane of the microscope such that multiple copies of the image are generated at different angles. Some of the orders are collected by the first lens (L1), which is placed a distance f_1 from the grating, producing the

Figure 9

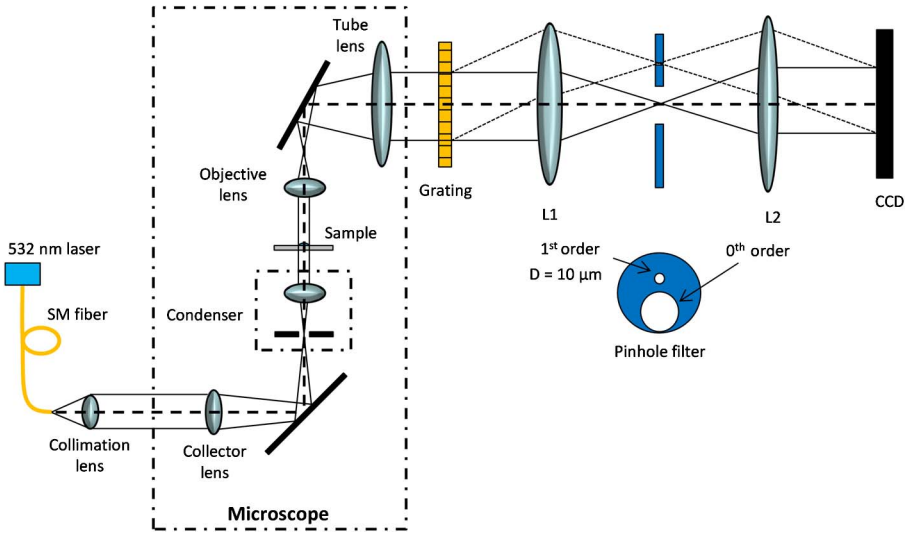

Laser DPM setup operating in transmission.

Fourier transform of the image at a distance f_1 behind the lens. Here, the 1st order beam is filtered down using a 10 μm diameter pinhole, such that after passing through the second lens (L2) this field approaches a plane wave. This beam serves as our reference for the interferometer. A large semicircle allows the full 0th order to pass through the filter without introducing any additional windowing effects. Using the 0th order as the image prevents unnecessary aberrations since it passes through the center of the lenses along the optical axis. A blazed grating was employed where the $+1$ order is brightest. This way, after the filter, the intensities of the two orders are closely matched, ensuring optimal fringe visibility. A second $2f$ system with a different focal length is used to perform another spatial Fourier transform reproducing the image at the CCD plane. The two beams from the Fourier plane interfere to produce an interferogram in the camera plane. The interferogram is a spatially modulated signal, which allows us to extract the phase information via a Hilbert transform [41] and reconstruct the surface profile [49,50,54].

3.1b. Applications

3.1b.1. Live red blood cell imaging. Laser DPM in transmission mode is suitable for quantitatively imaging live RBCs. We imaged live RBCs diluted with Coulter LH series diluent (Beckman–Coulter) to a concentration of 0.2% whole blood in solution. Figure 8(a) is the interferogram obtained with DPM in transmission mode, whereas Figs. 8(d) and 8(e) are the quantitative phases obtained via the derivative method [52] and Hilbert transform [41], respectively. In Sections 3.1b.3 and 3.1b.4 we will show important applications of RBC phase images obtained with DPM.

3.1b.2. Live neuron cell imaging. Further, laser DPM is also found to be quite useful in imaging other types of live cells. We can directly get the optical path difference map (more commonly, the phase map) provided by the sample, which is linearly proportional to refractive index and thickness of the sample. We can get one of these from the known value of the other. Also, we can use this phase

Figure 10

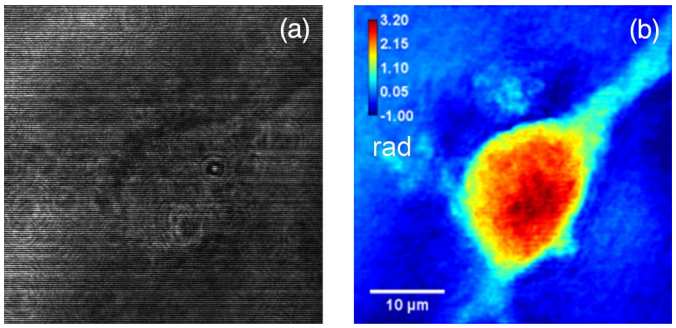

Live neuron cell imaging. (a) Transmission DPM interferogram of a live neuron cell. (b) Reconstructed phase with Hilbert transform. Color bar shows the phase in radians.

map to get dry mass or the nonaqueous content of the sample using a linear relation [31]. To show the capability of the system, we have imaged live rat neuron cells. Figure 10(a) shows the interferogram obtained by the DPM system, and Fig. 10(b) shows the reconstructed quantitative phase of a neuron cell. The color bar shows the phase in radians.

3.1b.3. Red blood cell mechanics. Deformability of the RBC in microvasculature determines the cell's ability to survive the physical demands of circulation, as well as the cell's ability to transport oxygen in the body [55]. It is interesting that RBCs must periodically pass a deformability test by being forced to squeeze through narrow passages, i.e., sinuses in the spleen. If a RBC fails this mechanical assessment, it is then destroyed and removed from circulation by macrophages [56]. To understand the mechanics of live RBCs quantitatively, one requires sensitive probes of their structure at the nanoscale [57–65]. Such investigation promises new insights into the etiology of a number of human diseases [66]. In the healthy individual, these cells withstand repeated, large-amplitude mechanical deformations as they circulate through the microvasculature. Throughout their 120-day lifespan, the RBCs' mechanical integrity degrades, and ultimately they are replaced by new circulating RBCs. Certain pathological conditions, such as spherocytosis, malaria, and sickle cell disease, cause changes in both the equilibrium shape and mechanics of RBCs, which impact their transport function. Thus, understanding the microrheology of RBCs is of great interest from both a basic science and a clinical point of view.

Lacking a conventional 3D cytoskeleton structure, RBCs maintain their shape and mechanical integrity through a spectrin-dominated triangular 2D network associated with the cytosolic side of their plasma membrane [67]. This semi-flexible filament network confers shear and bulk moduli to the composite membrane structure [68]. The fluid lipid bilayer is thought to be the principal contributor to the bending or curvature modulus of the composite membrane. Little is known about the molecular and structural transformations that take place in the membrane and spectrin network during the cell's response to pathophysiological conditions, which are accompanied by changes in RBC mechanics.

A number of techniques have been used recently to study the rheology of live cells [57,59,66]. However, *dynamic* frequency-dependent knowledge of RBC mechanics is currently very limited [69]. RBC thermal fluctuations

("flickering") have been studied for more than a century [70] to better understand the interaction between the lipid bilayer and the cytoskeleton [42,71–73]. Fluctuations in the phospholipid bilayer and attached spectrin network are known to be influenced by cytoskeletal defects, stress, and actin–spectrin dissociations arising from metabolic activity linked to adenosine-5 -triphosphate (ATP) concentration [59,73–76]. Nevertheless, quantifying these motions is experimentally challenging, and reliable spatial and temporal data are desirable [72,77–79].

In 2010, Park *et al.* from MIT reported "Measurement of red blood cell mechanics during morphological changes" [80]. Blood samples were prepared as described in Ref. [81]. The RBCs were then placed between coverslips and imaged without additional preparation. The samples were primarily composed of RBCs with the typical discocytic shapes (DCs) but also contained cells with abnormal morphology, which formed spontaneously in the suspension, such as echinocytes (ECs, cells with a spiculated shape) and spherocytes (SCs, cells that had maintained a roughly spherical shape). By taking into account the free energy contributions of both the bilayer and cytoskeleton, these morphological changes have been successfully modeled [82].

The standard description of a RBC treats the membrane as a flat surface; in reality the membrane of a RBC is curved and has the compact topology of a sphere. The Levine group at University of California, Los Angeles, developed a model that takes into account this geometrical effect and incorporates the curvature and topology of a RBC within the fluctuation analysis (for details on this theory, see Ref. [83]). The undulatory dynamics of a RBC is probed experimentally by measuring the spatial and temporal correlations of the out-of-plane fluctuations of the membrane. Theoretically, these correlations can be calculated using the response matrix χ and the fluctuation–dissipation theorem [84].

We used the new model of RBC mechanics over the commonly occurring discocyte–echinocyte–spherocyte (DC-EC-SC) shape transition [Figs. 11(a), 11(c)] [80]. From measurements of dynamic fluctuations on RBC membranes, we extracted the mechanical properties of the composite membrane structure. Subtraction of the instant thickness map from the averaged thickness map provides the instantaneous displacement map of the RBC membranes (Fig. 11, right column). Over the morphological transition from DC to SC, the RMS amplitude of equilibrium membrane height fluctuations $\sqrt{\langle \Delta h^2 \rangle}$ decreases progressively from 134 nm (DCs) to 92 nm (ECs) and 35 nm (SCs), indicating an increase in cell stiffness.

To extract the material properties of the RBC, we fit our model to the measured correlation function $\Lambda(\rho, \tau)$ by adjusting the following parameters: the shear μ and bulk K moduli of the spectrin network, the bending modulus κ of the lipid bilayer, the viscosities of the cytosol η_c and the surrounding solvent η_s, and the radius of the sphere R. We constrain our fits by setting R to the average radius of curvature of the RBC obtained directly from the data and fixing the viscosities for all datasets to be $\eta_s = 1.2$ mPa · s, $\eta_s = 5.5$ mPa · s [77,78]. Finally, for a triangular elastic network we expect $\mu = \lambda$, so we set $K = 2\mu$ [77]. These values are in general agreement with those expected for a phospholipid bilayer $(5 \quad 20) \times k_B T$ [79]. The increase in bending modulus suggests changes in the composition of the lipid membrane. We measured directly the change in surface area of RBCs during the transition from DC to SC morphologies and

Figure 11

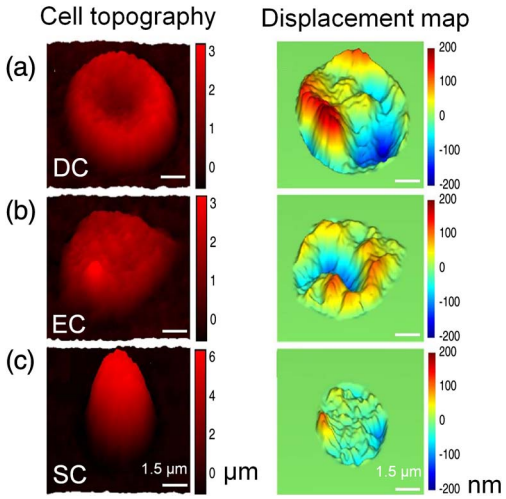

RBC topography (left column) and instantaneous displacement maps (right column) for (a) a discocyte, (b) an echinocyte, and (c) a spherocyte, as indicated by DC, EC, and SC, respectively. Adapted from Park *et al.*, "Measurement of red blood cell mechanics during morphological changes," Proc. Natl. Acad. Sci. U.S.A. **107**, 6731–6736 (2010) [80] with permission.

found a 31% decrease in surface area (not accounting for surface area stored in fluctuations). This surface area decrease must be accompanied by a loss of lipids, via membrane blebbing and microvesiculation. Thus, there is evidence that a significant change in lipid composition of the RBC bilayer accompanies the morphological changes from DC to EC and SC. It is thought that these changes in lipid composition generate the observed changes in the bending modulus. These data suggest that there are essentially two independent conformations of the spectrin network: a soft configuration ($\mu \cong 7\ \mu Nm^{-1}$) and a stiff one ($\mu \cong 13\ \mu Nm^{-1}$). Essentially all DCs have the soft configuration, but the morphological transition to EC and then SC promotes the transition to the stiff network configuration. We propose that the observed morphological changes must be accompanied by modifications of the spectrin elasticity, the connectivity of the network, or the network's attachment to the lipid bilayer.

3.1b.4. Imaging of malaria-infected RBCs. Malaria is an infectious disease caused by a eukaryotic protist of the genus *Plasmodium* [67,85]. Malaria is naturally transmitted by the bite of a female *Anopheles* mosquito. This disease is widespread in tropical and subtropical regions, including parts of the Americas (22 countries), Asia, and Africa. There are approximately 350–500 million cases of malaria per year, killing between 1 and 3 million people, the majority of whom are young children in sub-Saharan Africa [85]. In severe cases the disease worsens, leading to hallucinations, coma, and death. Five species of the *Plasmodium* parasite can infect humans; the most serious forms of the disease are caused by *Plasmodium falciparum*. Malaria caused by *Plasmodium vivax, Plasmodium ovale*, and *Plasmodium malariae* causes milder disease in humans that is not generally fatal.

During the intra-erythrocytic (RBC) development, the malaria parasite *Plasmodium falciparum* causes structural, biochemical, and mechanical changes to host RBCs [86]. Major structural changes include the growing of vacuole of parasites

in cytoplasm of host RBCs, loss of cell volume, and the appearance of small, nanoscale protrusions, called "knobs" or "blebs," on the membrane surface [87]. From the biochemical standpoint, a considerable amount of hemoglobin (Hb) is digested by parasites during intra-erythrocytic development and converted into insoluble polymerized forms of heme, known as hemozoin [88,89]. Hemozoin

Figure 12

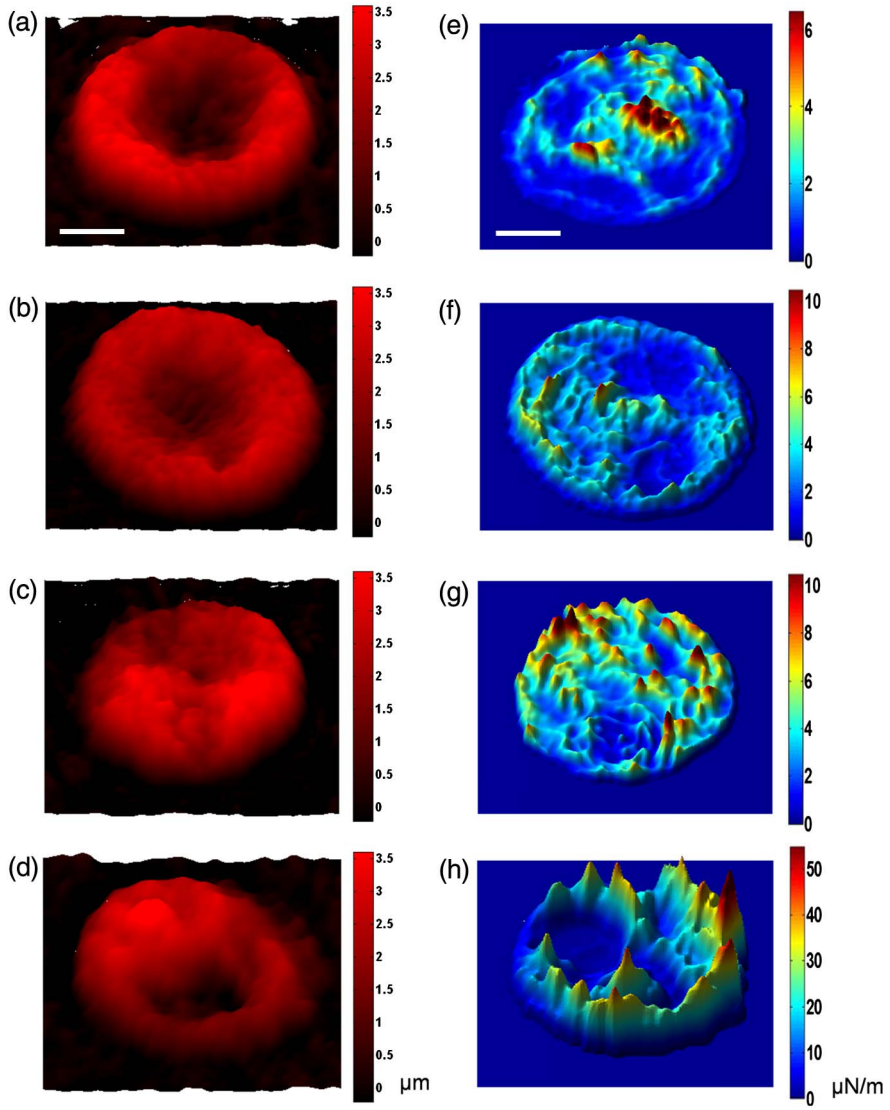

Topographic images and effective elastic constant maps of *Pf*-RBCs. (a) and (e) Healthy RBC. (b) and (f) Ring stage. (c) and (g) Trophozoite stage. (d) and (h) Schizont stage. The topographic images in (a)–(d) are the instant thickness map of *Pf*-RBCs. The effective elastic constant maps were calculated from the RMS displacement of the thermal membrane fluctuations in the *Pf*-RBC membranes. Black arrows indicate the location of *P. falciparum*, and the gray arrows indicate the location of hemozoin. (Scale bar, 1.5 μm.) Adapted with permission from Park *et al.*, "Refractive index maps and membrane dynamics of human red blood cells parasitized by *Plasmodium falciparum*," Proc. Natl. Acad. Sci. U.S.A. **105**, 13730 (2008) [94]. Copyright 2008 National Academy of Sciences, U.S.A.

appears as brown crystals in the vacuole of parasites in later maturation stages of *P. falciparum*-invaded human RBCs (*Pf*-RBCs) [67]. Two major mechanical modifications are loss of RBC deformability [90–92] and increased cytoadherence of the invaded RBC membrane to vascular endothelium and other RBCs [93]. These changes lead to sequestration of RBCs in microvasculature in the later stages of parasite development, which is linked to vital organ dysfunction in severe malaria. In the earlier stage, where deformability occurs, *Pf*-RBCs continue to circulate in the blood stream despite infection.

In 2008, the MIT groups led by Suresh and Feld collaborated on using DPM to study the modifications in RBC dynamics produced by the onset and development of malaria [94]. To investigate morphological changes of *Pf*-RBCs, we measured the instantaneous thickness profile, $h(x, y, t_0)$ of cells [94]. Figures 12(a)–12(d) show topographic images of healthy and *Pf*-RBCs at all stages of development. The effective stiffness map of the cell, $k_e(x, y)$, is obtained at each point on the cell, assuming an elastic restoring force associated with the membrane:

$$k_e(x, y) = k_B T / \langle \Delta h(x, y)^2 \rangle, \tag{3.1-1}$$

where k_B is the Boltzmann constant, T the absolute temperature, and $\langle \Delta h(x, y)^2 \rangle$ the mean-squared displacement. Representative k_e maps of RBCs at the indicated stages of parasite development are shown in Figs. 12(e)–12(g). The map of instantaneous displacement of cell membrane fluctuation, $\Delta h(x, y, t)$, was obtained by subtracting time-averaged cell shape from each thickness map in the series.

These results demonstrate a potentially useful avenue for exploiting the nanoscale and quantitative features of QPI for measuring cell membrane fluctuations, which, in turn, can report on the onset and progression of pathological states.

3.2. Reflection Mode

3.2a. Setup

Figure 13 shows a schematic of the laser DPM system operating in reflection mode (epi-DPM). The prefix *epi* stands for epi-illumination and stems from the fact that the light is collected from the same side of the sample where it is incident. The only difference between reflection and transmission mode is in the light path within the microscope. In reflection mode, the collimated beam entering the back of the microscope passes through a collector lens and is focused onto the back focal plane of the objective. The objective lens then creates a collimated beam in the sample plane. Scattered and unscattered light reflected by the sample are collected by the objective and again focused in its back focal plane. A beam splitter redirects the light through a tube lens, creating a collimated beam containing the image at the output image plane of the microscope. The laser setup at the input and the DPM setup at the output remain unchanged.

3.2b. Applications

3.2b.1. Watching semiconductors etch. The spatial and temporal sensitivities discussed in Section 2 underscore the capability of epi-DPM to accurately monitor dynamics at the nanoscale. To exploit this feature, we captured the dynamics

Figure 13

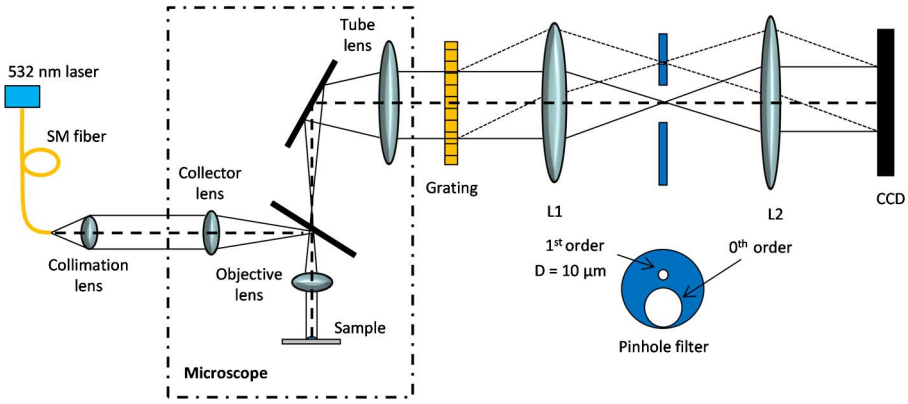

Laser DPM setup operating in reflection mode.

of the wet etching process in real time. The sample was prepared as follows. First, plasma-enhanced chemical vapor deposition (PECVD) was used to deposit 50 nm of silicon dioxide onto an n^+GaAs wafer. The University of Illinois logo was then patterned and transferred onto the oxide using a standard SPR511A photoresist recipe followed by reactive ion etching with Freon gases.

The prepared sample was placed upside down in a Petri dish and propped up on a glass pedestal. This allows the etchant to diffuse under the inverted sample while imaging from underneath. 10 mL of deionized water was placed into the Petri dish and the sample was brought into focus. A solution of H_3PO_4:H_2O_2 was then pipetted into the dish and 400 images were captured at 8.93 frames/s for a total of 44.8 s.

Figure 14 shows selected video frames that contain the etch depth at each pixel. Initially the thin oxide mask is difficult to observe due to the poor index contrast between the oxide ($n = 1.55$) and etchant ($n = 1.33$). It took approximately 10 s for the etchant to diffuse into the FOV and begin etching the logo. The bulk of the etchant first enters into the top-left portion of the FOV and diffuses diagonally toward the bottom-right corner. The spatial inhomogeneity is captured as the etch evolves. Upon closer inspection, it can be seen that the narrow regions of the logo etch at a slower rate. This occurs because the local etchant is used up quickly in the narrow trenches and the resulting etch becomes diffusion-limited as new etchant must diffuse into the region and replace the byproducts. In the open regions where the etchant is already present, the process is reaction-limited and etching occurs at a faster rate. Note that the etch rate of SiO_2 deposited with PECVD using such a dilute solution is less than 1 nm/min, and, given the short etch times, the amount of oxide etching can be considered negligible [95].

The final structure after etching was complete is shown in Fig. 15(a), while Fig. 15(b) illustrates the time-resolved etch depth profile at selected points within the FOV, as indicated by markers in the adjacent figure. Since the etch depth is captured at each pixel over time, we essentially have four-dimensional information at our disposal. This allows us to compute the instantaneous etch rates at each pixel at a given time instance. Figures 15(c)–15(e) show the etch rate across the entire FOV at different moments during the process, while Fig. 15(f) displays the overall average etch rate. These results reveal important details about the etching process. For example, we can see that the etch rate may

Figure 14

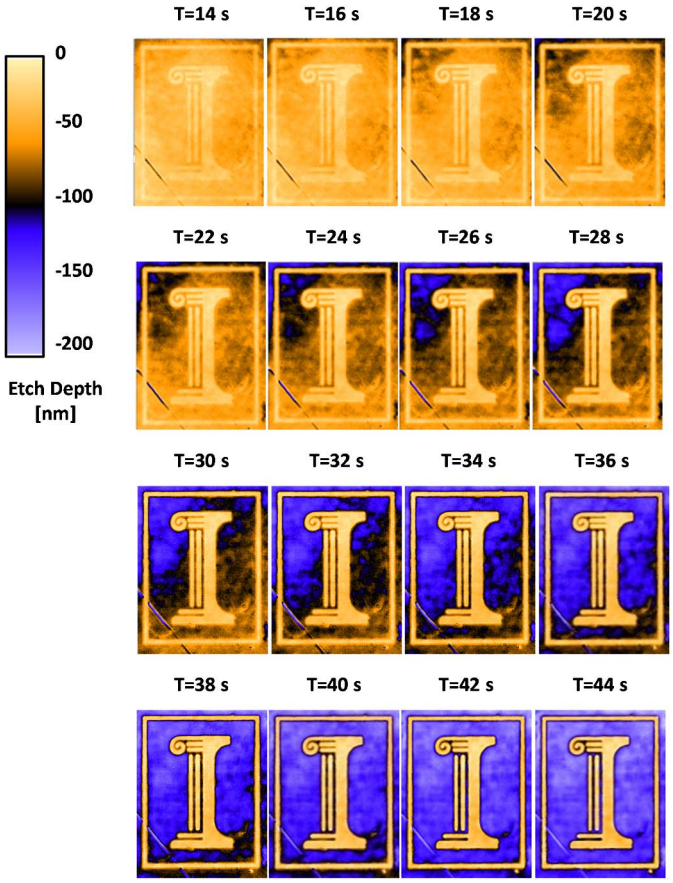

Real-time imaging during wet etching of the University of Illinois logo. A 5× objective was used for monitoring the etch, resulting in a FOV of 320 μm × 240 μm for each of the images shown. The video was acquired at 8.93 frames/s. It took roughly 10 s for the etchant to diffuse into the FOV and begin etching. Still frames over a 30 s interval from 14–44 s are displayed, showing the dynamics of the etching process. Diffusion of the etchant from the top-left corner to the bottom-right corner is observed. Adapted from [50].

vary by several nanometers/second at unmasked points separated by only a few micrometers in space at a fixed moment in time or at times separated by only a few seconds at a fixed point in space. These nonuniformities are due to fluctuations in the concentration of the etching solution [50].

The epi-DPM technique has demonstrated the ability to monitor wet etching *in situ* with nanometer accuracy. This method could potentially be used to create a multi-user cleanroom tool for wet etching that would allow the user to observe all of this information during etching, which could greatly improve the quality of the etch as well as the overall yield. Furthermore, the ability to accurately measure these inhomogeneities in real time may provide the means to correct the fabrication on-the-fly by perfusing the etching chamber with an adjustable etchant concentration [50].

3.2b.2. Digital projection photochemical etching. Photochemical etching (PC etching) is a low-cost semiconductor fabrication technique with the ability

Figure 15

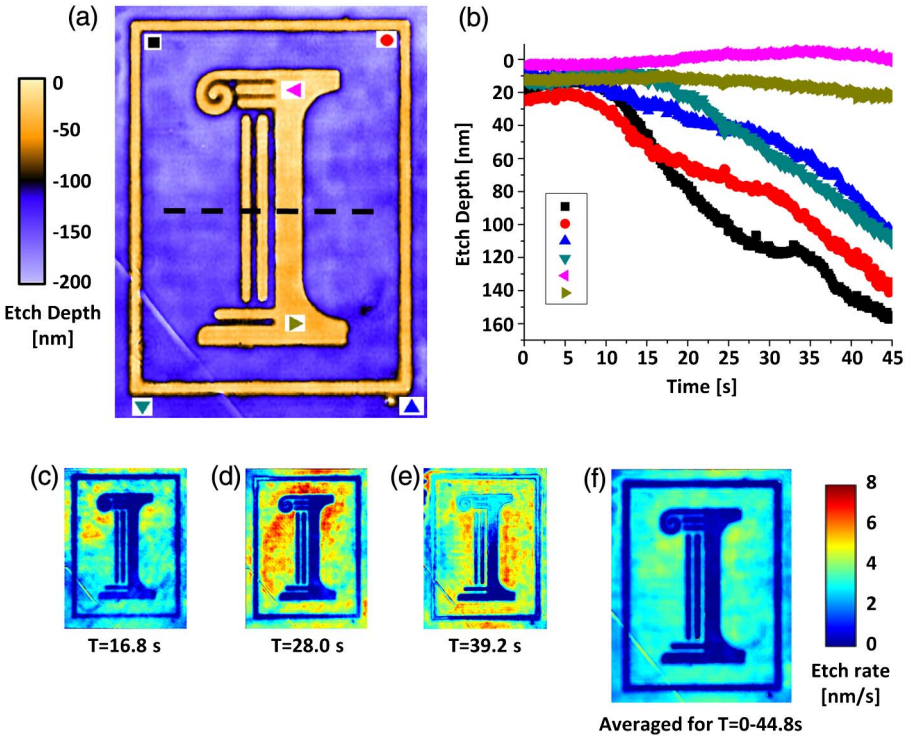

Analysis of real-time etching dynamics. (a) Final depth profile after etching was completed. (b) Plot of etching depths over time to show variation of depths and etch rates at points indicated in (f). (c)–(e) Etch rates at each pixel across the FOV at frame 150 (16.8 s), frame 250 (28.0 s), and frame 350 (39.2 s). (f) Overall etch rate averaged over the entire etch process. The etch rate may vary by several nanometers/second over the FOV at any given time, but average out over time. Adapted from [50].

to etch structures with gray-scale topography. When light with sufficient energy is absorbed near the surface of a semiconductor material, minority carriers are generated that can then diffuse to the surface and act as a catalyst in the etching process. Our lab has recently developed a technique called digital projection photochemical etching [96]. Here, we can use a standard classroom projector to focus a gray-scale image into the sample plane and use light itself as the mask for etching. This alleviates the need for standard photolithography, which requires spin coating photoresist, aligning and exposing, and developing. With digital projection PC etching we can etch gray-scale structures that are difficult to fabricate using conventional photolithography and even etch multilevel structures in a single processing step [96]. The color (or wavelength) of the projector light, as well its intensity, can be adjusted to control etch rates and even provide both spatial and material selectivity. The projected pattern may also be adjusted dynamically throughout the etching process.

Figure 16 shows the experimental setup for PC etching, which is integrated into the DPM workstation [96]. This allows us to measure the dimensions of the etched structures on site in a completely noninvasive manner. This is not possible with scanning electron microscopy (SEM), transmission electron microscopy, atomic force microscopy, or other similar inspection methods [50,97,98].

Figure 16

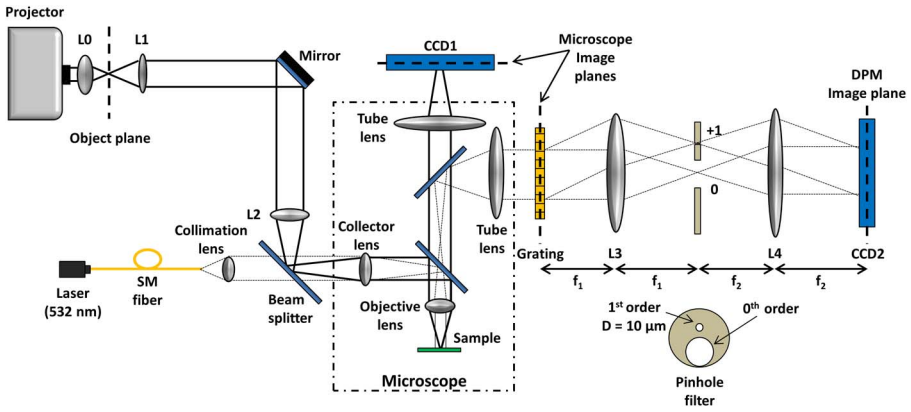

Digital projection PC etching system. Illustration showing the integration of our newly developed digital projection PC etching and epi-DPM methods. The bold solid lines represent the light path from the projector, which was focused on the sample and aligned using CCD1. The epi-DPM system was used to measure the height of features on the sample using CCD2. The light path for epi-DPM is indicated by the dotted lines. Adapted from [96].

The bold solid lines represent the light path from the projector, where the mask pattern was focused upon the sample's surface and aligned using CCD1. The epi-DPM system was used to measure the height of features on the sample using CCD2. The light path for epi-DPM is indicated by the dotted lines.

The etch rates for red, green, and blue light at different intensities were determined by projecting a mask pattern with eight 30 μm squares containing gray levels of 32, 64, 96, 128, 160, 192, 224, and 255 for each color and performing a 30 s etch [96]. The mean and standard deviation of the measured etch depth inside each square were recorded, and the differential etch rates as a function of the gray level for each color component were calculated using the recorded etch time and etch depths. The background (dark) etch rate was then measured, which allowed us to determine the absolute etch rate for the different colors and gray levels. These rates were used to compute the etch times required for a desired etch depth (or height) in subsequent etches [96].

To characterize the system, we measured the etch feature resolution and edge resolution of etched structures, as well as the spatial and temporal noise of the epi-DPM imaging system. To test the resolution of the PC etching process, mask patterns containing selected portions of the USAF-1951 target with feature sizes ranging from 16 to 1.2 μm were created for each color [96]. Figure 17(a) shows an image captured using a 20×, 0.5 NA objective (1.3 μm resolution) and shows the collection of lines taken from a selected portion of the etched target. Figure 17(b) contains a cross section taken along the horizontal lines (2 μm × 10 μm), showing that we are able to clearly resolve the 2 μm features from the resolution target. Note that three peaks are also faintly visible even at 1.4 μm. The etching resolution comprises three components: the diffraction limit of light projected into the sample plane, the diffusion of carriers as a result of the PC etching process (diffusion length for n^+GaAs at room temperature is 1.1 μm [99]), and aberrations and imperfections in the optical system. According to

Abbe's formula, the optical resolution limit for red, green, and blue light using the 10×, 0.2 LD objective is 1.9, 1.6, and 1.4 μm, respectively. Further broadening in the features is a result of the diffusion of carriers as well as optical imperfections in the setup. There are also slight discrepancies between the vertical and horizontal resolutions, which are due to the rectangular geometry of the RGB subpixels inside the projector. The resolution can be further improved by using a higher NA objective.

Figure 17(c) contains an epi-DPM height map of our standard control sample, a micropillar, that was etched using our technique. A mask pattern was used with gray levels of 0 and 136 for the pillar and background, respectively. PC etching was performed for 60 s, resulting in a mean height of 304.9 nm. It was calibrated to have a 100 μm diameter and a height of 300 nm. Figure 17(d) contains a cross section of the pillar in Fig. 17(c), showing that the resulting width and height were 100 μm and 304.9 nm, respectively. The edge resolution was measured to be $\varepsilon = \Delta x/\Delta y = 30$, which is due to the diffusion of carriers during the PC etching process. Note that, for a standard isotropic wet etch, the edge resolution is $\varepsilon = \Delta x/\Delta y = -1$ since there is 1 nm of undercutting per 1 nm of etching. This broadening effect is currently the primary limitation of this new technique, but may be alleviated using computation photolithography, which prewarps the mask pattern in order to achieve more vertical sidewalls.

Figure 17

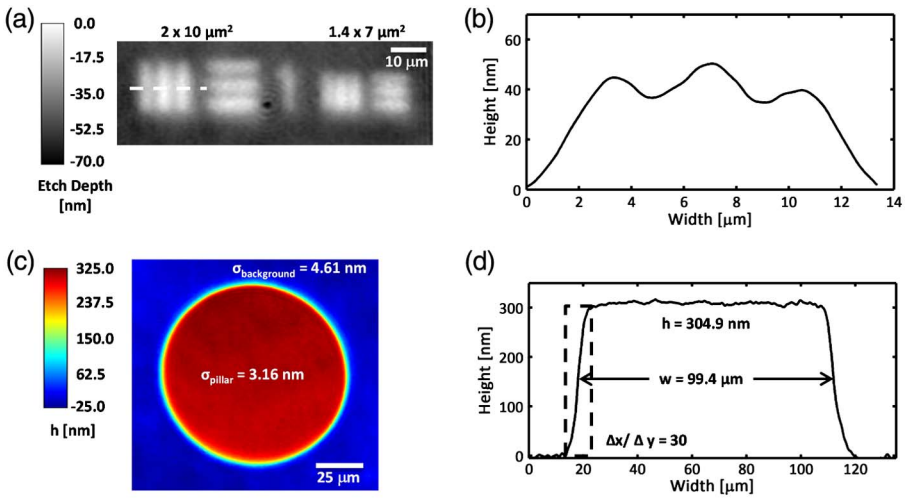

System characterization. (a) epi-DPM image of horizontal and vertical lines etched using the USAF-1951 resolution target. Image was captured using a 20×, NA = 0.5 objective (650 nm lateral resolution). (b) Cross section of horizontal lines taken along the dotted line in (c). Based on this resolution test, the etch feature resolution using our PC etching setup is approximately 2 μm. (c) DPM height map of a PC etched micropillar. Mask patterns with gray levels of 0 and 136 were used for the pillar and background, respectively. PC etching was performed for 60 s, resulting in a mean height of 304.9 nm. It was calibrated to have a 100 μm diameter and a height of 300 nm. (d) Cross section of the pillar in (c) showing the dimensions and edge resolution. Adapted from [96].

Figure 18(a) shows a height map of stacked cubes that were fabricated in a single etch step [96]. A projected image with gray levels of 0, 60, and 78 was used for the mask pattern. PC etching was performed for 33 s, resulting in mean heights of 0, 50.7, and 101.6 nm. The etched structure was calibrated to have widths of 150 and 75 μm with heights of 0, 50, and 100 nm. The corresponding histogram is displayed in Fig. 18(b), which indicates the mean height of each of the three layers and illustrates the high degree of process control and repeatability. Multiple structures can also be etched simultaneously, as we have illustrated in Fig. 18(c), which contains the surface profile of a microlens array etched using our technique. The diameters of the microlenses were calibrated to be 100 μm with a pitch of 120 μm. Figure 18(d) shows a comparison between the projected pattern and the etched structure. Here, a cross section of the mask pattern is overlaid with both horizontal and vertical slices from the etched micropillar

Figure 18

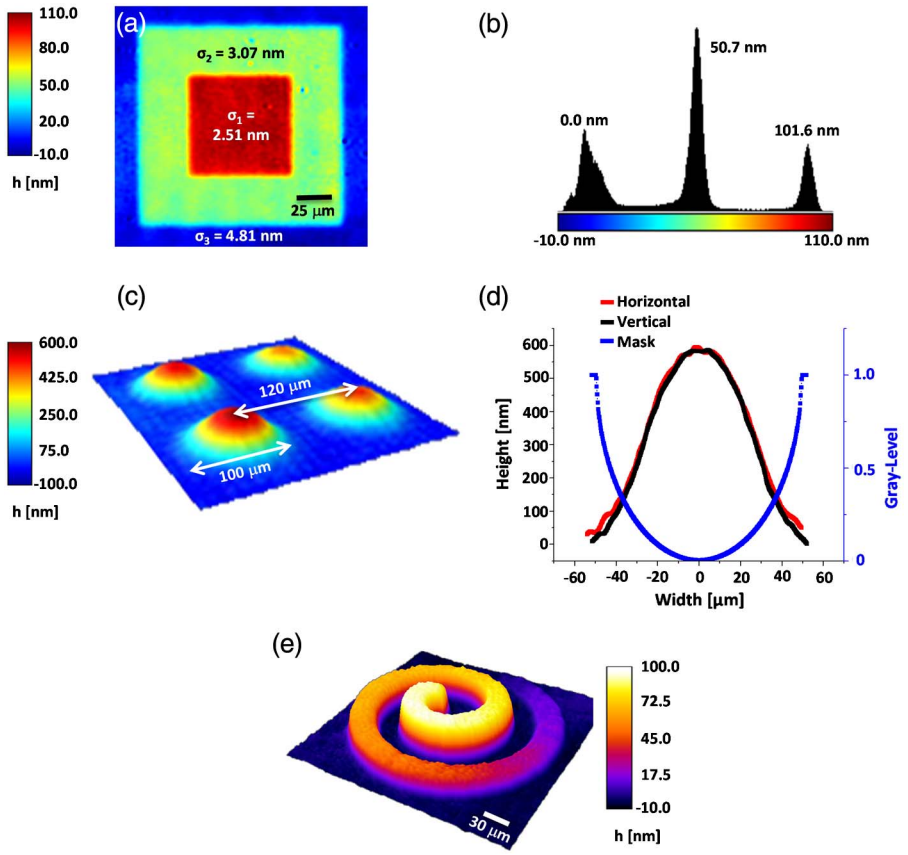

Etched structures. (a) DPM height image of stacked cubes. A projected image with gray levels of 0, 60, and 78 were used for the mask pattern. PC etching was performed for 33 s, resulting in mean heights of 0, 50.7, and 101.6 nm. It was calibrated to have widths of 150 and 75 μm with heights of 0, 50, and 100 nm. (b) Histogram of image in (c) showing the heights of the three levels. (c) Topographical reconstruction of a microlens array fabricated using PC etching. (d) Comparison between s cross section of the projected mask pattern and horizontal and vertical cross sections from an etched microlens. (e) Topographical profile of PC etched Archimedean spiral. Adapted from [50,96].

image. The mask appears inverted because the dark regions etch most slowly, forming the top of the microlens, while the brighter regions of the mask produce the perimeter of the lens. To further illustrate the strengths of the technique, an Archimedean spiral was fabricated using a continuous gray-scale mask pattern. The gray-level values decreased linearly around the spiral from 96 down to 0. The maximum height and width were calibrated to be 100 nm and 30 μm, respectively. Figure 18(e) shows the surface topography of an etched spiral. Note that this type of structure is very difficult to fabricate using standard photolithography. In fact, the spiral would need to be broken up into many discrete steps, each requiring a separate processing step. Note that this structure was etched in 33 s. To quantify the roughness of the etched structures, the standard deviations were recorded for the flat regions of the micropillar and multilevel cubes, as reported in Figs. 17(c) and 18(a), respectively. These measurements show that the roughness is less than 5 nm for all cases, which is comparable to the roughness of a standard wet etch done under typical cleanroom conditions [96].

Digital projection PC etching is capable of fabricating gray-scale structures that are otherwise difficult to obtain using standard photolithography and is capable of etching multilevel structures in a single processing step. The etch rates can be determined for a given material/etchant combination by performing the etch rate test described above [96]. The etch feature resolution is between 1.68 and 2.38 μm for the three colors as determined by etching selected portions of the USAF-1951 target. Furthermore, using this integrated setup, dimensions of the etched structures can be measured on site in a completely nondestructive manner.

3.2b.3. Semiconductor wafer defect detection. In-line detection of killer defects in patterned wafers has been a grand challenge of the International Technology Roadmap for Semiconductors (ITRS). Currently, the semiconductor industry is using the 22 nm node technology; thus, detecting defects that are smaller than 22 nm in size is very critical for semiconductor manufacturers to maximize their yield. To detect defects in 22 nm node wafers, deep ultraviolet lasers and high-order harmonic sources have been proposed [100,101]. In fact, the ultimate limiting factor in an imaging system is the signal-to-noise contrast [102]. DPM has very low noise as discussed earlier, so we adapted the epi-DPM system to measure both the phase and amplitude of the scattered field from an intentional defect array wafer (IDA) provided by SEMATECH. The IDA wafer consists of 100 μm × 100 μm 2D arrays. Within each array, there are straight lines that are 240 or 120 nm in length and 22 nm wide. In the center of the 2D array, there is a printed defect; see Ref. [102] for more details on the IDA wafer and defects. Figure 19 schematically shows different types of defects for the IDA wafer, specifically, an isolated dot defect, a perpendicular bridge defect, and a parallel bridge defect. The defect width can vary in size, which scales against 22 nm.

For each 2D array, we collect a sequence of interferograms while mechanically translating the wafer with 1 μm stepping size in the line structure direction in the plane parallel to its surface. For each interferogram frame, the phase and amplitude images are retrieved. Since the defect is very small, the various noises in a single frame can still degrade the defect signal contrast. To improve signal contrast, we developed a sequence of image postprocessing methods [102,103]. After image processing, we stitch all the frames together to produce a stretched

Figure 19

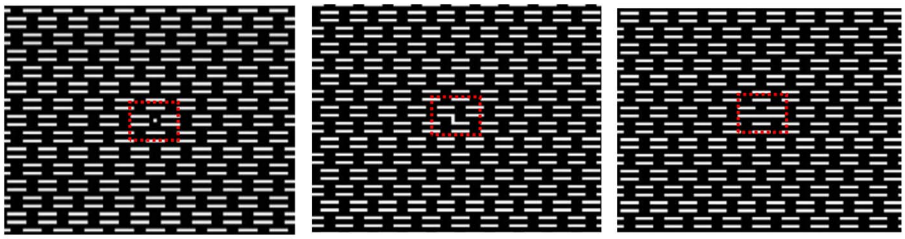

Illustration of different defect types. (a) An isolated defect, (b) a perpendicular bridge defect, and (c) a parallel bridge defect. Adapted from Zhou *et al.*, "22 nm node wafer inspection using diffraction phase microscopy and image post-processing," Proc. SPIE **8681**, 8610G (2013) [103] with permission from SPIE.

panoramic image where the noise is significantly decreased and the signal from the defect is stabilized. In Figs. 20(a) and 20(b), we show the stretched amplitude and phase images for a 20 nm × 110 nm parallel bridge defect, respectively, as an example. In both images, the defect can be clearly observed with no false alarms in the 25 μm × 80 μm FOV. Using the same techniques, other types of defect were also detected. The minimum defects we detected were 35 nm × 70 nm for an isolated dot defect, 20 nm × 110 nm for a parallel bridge defect, and 20 nm × 110 nm for a vertical bridge defect. These detection results were confirmed with SEM.

Figure 20

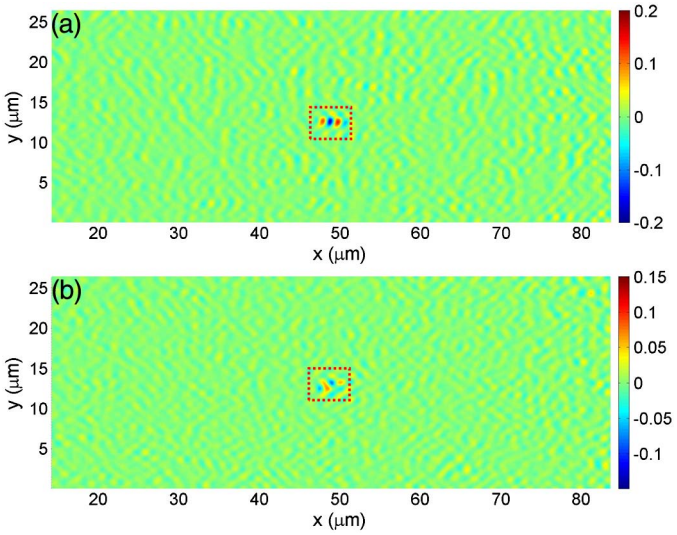

Stretched image using moving averaging. (a) Stretched amplitude image and (b) stretched phase image. In each stretched image, the location of the defect is marked by a red box. Adapted from Zhou *et al.*, "22 nm node wafer inspection using diffraction phase microscopy and image post-processing," Proc. SPIE **8681**, 8610G (2013) [103] with permission from SPIE.

4. White-Light DPM

Because of the high coherence of the laser illumination, laser DPM images suffer from speckles, which ultimately degrade the spatial phase sensitivity. We have recently developed white-light diffraction phase microscopy (wDPM), which uses white-light illumination and, thus, improves the overall spatiotemporal noise of the system [54]. DPM imaging systems using white-light illumination typically exhibit lower noise than their laser counterparts. This is a result of the lower coherence (both spatially and temporally), which reduces noise mechanisms, such as laser speckle. On the other hand, without proper spatial filtering, white-light DPM systems can exhibit aberrations and artifacts, like the halo effect, that are not present in laser DPM systems. Each type of illumination has its own strengths and weaknesses. Currently, it appears that laser DPM works well for material science applications where structural features have large lateral extent and may also have sharp edges, while white light is best suited for biological applications where the features have much smaller lateral extent and are smoother [104,105].

4.1. Setup

White-light DPM is implemented as an add-on module to a commercial microscope (Axio Observer Z1, Zeiss). Figure 21 shows the experimental setup, where we employ spatially coherent white-light illumination, obtained from a halogen lamp commonly used in commercial microscopes. In wDPM, the reference beam is created by first closing down the NA of the condenser and then filtering the 0th order diffraction beam with a pinhole mask on the spatial light modulator (SLM), which matches with the aperture of the condenser. If the aperture is small enough, we expect to see a uniform reference beam. In our current configuration, the minimum aperture we can get is NA $= 0.09$. This results in a reference beam that is not perfectly uniform and is a low-pass-filtered version of the sample beam, which in turn can result in halos in the final reconstructed phase images.

Figure 21

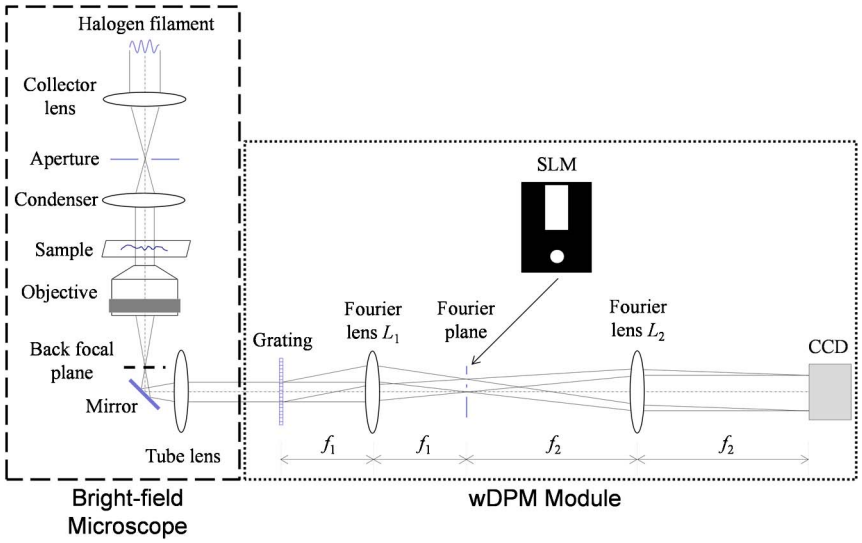

wDPM experimental setup.

This halo effect can be easily removed by reducing the condenser aperture size, however, at the expense of reducing the illumination power. Illumination power at the sample plane for this NA is 0.16 mW and for fully open condenser (NA = 0.55), it is 5.57 mW. As in DPM, at the image plane of the inverted microscope, we place a phase diffraction grating, which generates multiple diffraction orders containing full spatial information about the object. The 0th- and 1st-order beams are isolated at the Fourier plane generated by lens L1 using a SLM, as shown in Fig. 21. The 0th-order beam is spatially low-pass filtered such that only the DC component of the 0th order is passed, whereas the 1st order is completely passed. The diameter of the pinhole (zero order mask) at the Fourier plane is 200 μm and the rectangular opening (first order mask) has a size of 5 mm × 2 mm. The lens system L1–L2 forms a highly stable Mach–Zehnder interferometer. The 1st order is thus the imaging field and the 0th order plays the role of the reference field. Both beams are interfered and generate a spatially modulated interference image, which is then captured by a sCMOS camera (Hamamatsu ORCA Flash) at the image plane. The common-path geometry matches the optical path lengths for the sample and reference arms such that the alignment is independent of the wavelength and temporal coherence of the illumination source. The quantitative phase image associated with the sample is retrieved from a single camera recording via a spatial Hilbert transform [41]. We assume the live cells as phase objects, which is a common assumption in the field. This is a valid approximation as, for unstained cells, bright-field images show little to no contrast in intensity. The grating period (9 μm in the present case) was set to be smaller than the diffraction-limited spot of the microscopic imaging system at the grating plane. All the lenses are achromatic to minimize chromatic dispersion. Throughout our experiments, the microscope was equipped with a bright-field 40× (0.75 NA) objective. The L1–L2 lens system gives an additional magnification of $f_2/f_1 = 2.5$, such that the sinusoidal modulation of the image is sampled by 6 camera pixels per period.

To characterize the noise stability of our setup, we measured the phase of a time series of 256 background images of size 512 × 512, and the phase of a single background phase of the same size at a different spatial position. This background phase was then subtracted from all the previous temporally acquired phases to correct for any wavefront curvature, which is a constant associated with our instrument. Figure 22(a) shows the spatial noise of the wDPM system, obtained by subtracting two reconstructed phase images at two different FOV locations. The standard deviation of spatial noise in wDPM is a few times less than that obtained with DPM [Fig. 22(b)]. A more complete characterization of the spatiotemporal noise is obtained by numerically computing the spatial and temporal power spectrum as follows:

$$\phi(\mathbf{k},\omega) = \alpha\left|\iint_A \int_{-\infty}^{\infty} \delta\varphi(\mathbf{r},t)\mathbf{e}^{-i(\omega t-\mathbf{k}\cdot\mathbf{r})}\mathrm{d}t\mathrm{d}^2\mathbf{r}\right|^2, \tag{4.1-1}$$

where α is a normalization factor such that the area under $\phi(\mathbf{k},\omega)$ gives the variance of the spatiotemporal noise. This power spectral density describes the contribution to the variance of each temporal and spatial frequency component. Figures 22(c) and 22(d) illustrate this power spectral density along ω and k_x for $k_y = 0$ [Fig. 22(c)] and $k_y = 2\pi$ [Fig. 22(d)]. Our analysis underscores an important capability: by spatial and temporal bandpass filtering, the measurement noise can be reduced significantly. For example, measuring

Figure 22

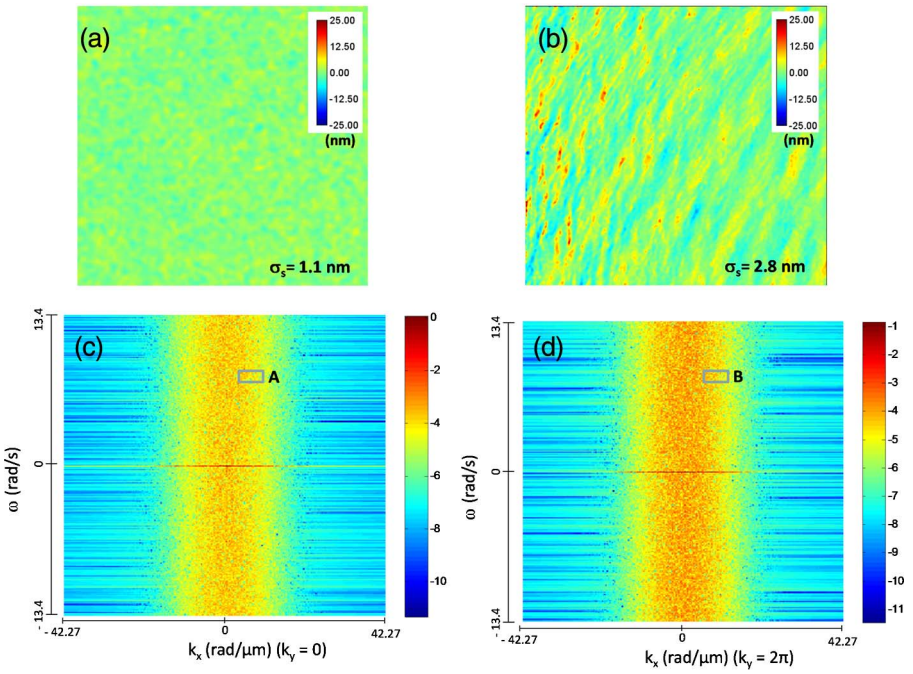

Noise stability of wDPM. (a) Spatial noise of wDPM. (b) Spatial noise of laser DPM. (c) and (d) Spatiotemporal power spectral density of wDPM in log scale at $k_y = 0$ and $k_y = 2\pi$, respectively; color bars in (c) and (d) are $\mathrm{nm}^2/[(\mathrm{rad/s}) \cdot (\mathrm{rad/\mu m})^2]$. Adapted from [54].

in the frequency range indicated by rectangles A and B in Figs. 22(c) and 22(d) gives optical path length noise levels of 0.11 and 0.07 nm, respectively. These remarkably low values are obtained for a spatial bandwidth of π rad/μm (0.5 μm spatial distance) in both directions and temporal bandwidth of 1 rad/s, which are easily achievable in practice. Thus, path-length changes of subangstrom scale can be measured by spatial and temporal filtering. It should be noted that the spatiotemporal filtering is in essence an averaging procedure and, therefore, wDPM's high acquisition rate can be traded for increased sensitivity.

4.2. Role of Coherence in wDPM

4.2a. Temporal Coherence

The temporal coherence length of white-light systems is typically on the order of a couple of micrometers, depending on both the source spectrum and the definition of coherence length used in the calculation [104,106]. The temporal coherence can be measured experimentally by first obtaining the spectrum of the source using a standard spectrometer. The source spectrum for a typical wDPM system is shown in Fig. 23(a). The autocorrelation function can then be obtained through a Fourier transform via the Wiener–Khintchine theorem [48,107]. The temporal coherence length can then be extracted as shown in Fig. 23(b). The temporal coherence length provides a benchmark for the maximum optical path-length difference over which we can obtain interference and thus accurately measure height using DPM. Most biological specimens in their typical imaging

Figure 23

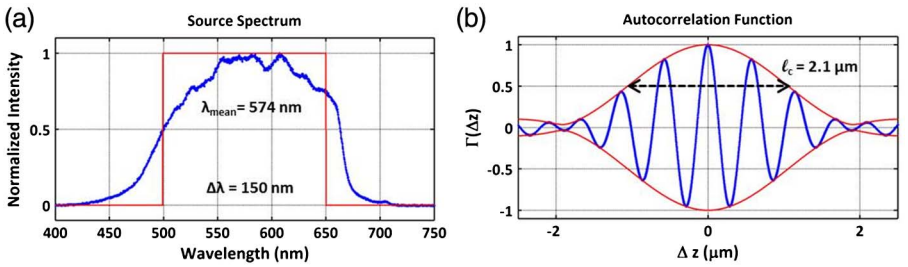

Temporal coherence of the wDPM imaging system. (a) Spectrum of the HAL 100 halogen lamp showing the power-equivalent bandwidth approximation. The center wavelength at a color temperature of 3200 K is 574 nm. This wavelength is used to convert the measured phase to height. (b) Temporal autocorrelation function and its envelope obtained via a Hilbert transform. The temporal coherence length obtained from the envelope is 2.1 μm. Adapted from [104].

media exhibit very low index contrast. For example, RBCs in Coulter solution have an index contrast of $\Delta n \approx 0.06$ [106]. At a given temporal coherence length, a lower Δn means that a larger height (i.e., $h_{\max} = \ell_c/\Delta n = 2.0/0.06 = 33$ μm), can be measured. Thus, the temporal coherence of the wDPM light source is at least 1 order of magnitude larger than what is needed to measure typical samples.

4.2b. Spatial Coherence

Our recent studies suggest a connection between the phase reductions in DPM and the degree of spatial coherence of the illumination [104,105]. When the illumination is fully coherent, the correct phase value is retrieved. Otherwise, the phase value will be increasingly underestimated when the degree of spatial coherence decreases. As pointed out in Refs. [104,105], the measured phase value $\phi(x,y)$ at transverse location (x,y) is related to the "true" phase value $\phi_o(x,y)$ through the following relation:

$$\phi(x,y) = \phi_o(x,y) - \arg[(\exp(i\phi_o) \circledcirc h)(x,y)], \tag{4.2-1}$$

where $h(x,y)$ is the spatial correlation function of the illumination at the sample plane. For illustration purposes, we consider two cases. First, when the illumination field on the sample is fully coherent, $h(x,y) \to c$ (a constant), $\phi(x,y) \to \phi_o(x,y) - c$. A normalization to zero out the phase value of the background will give $\phi(x,y) \to \phi_o(x,y)$. In this case, the correct phase value is returned irrespective of the sample's size and geometries. At the other extreme, when the illumination becomes fully incoherent, i.e., the condenser aperture is infinitely large, $h(x,y) \to \delta(x,y)$, we have $\phi(x,y) \to \phi_o(x,y) - \phi_o(x,y) = 0$, which establishes that the phase information is lost. Intermediates between these two extremes suggest reductions in the phase values between $\phi_o(x,y)$ and 0. This phase reduction also depends on the sample's transverse dimensions.

Figure 24 shows our measurement of 123 nm micropillars with different radii. We change the amount of spatial correlation by alternating the diameter of the condenser's aperture (and hence the NA of the condenser). It can be seen that the

Figure 24

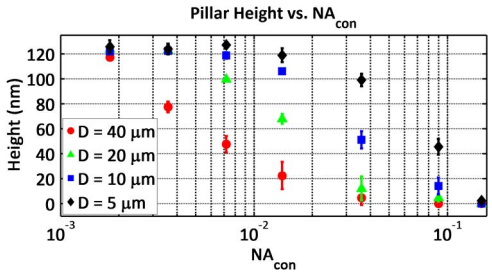

Measured phase value with respect to different sample size and various values of degree of spatial correlation. T. Nguyen, C. Edwards, L. L. Goddard, and G. Popescu are preparing a manuscript to be called "Quantitative phase imaging with partially coherent illumination," available from G. Popescu, gpopescu@illinois.edu.

height measurement converges to the correct value when the illumination becomes fully coherent irrespective of the sample size. The measured phase value reduces when the degree of coherence decreases with a decay rate that depends on the sample's dimensions. Samples with larger sizes tend to have faster decay rates than those of smaller ones.

4.3. Applications

4.3a. Red Blood Cell Membrane Fluctuation Measurement

We have used wDPM for imaging several live cells including RBCs. As wDPM gives low-noise phase images, it can be used for RBC membrane fluctuation measurement. For this, we captured 512 images of individual RBCs at 50 Hz with a bright-field objective (20×, 0.8 NA). From this time-lapse sequence, we obtained the average cell thickness map to create a binary mask to avoid the contribution outside the cell. Next we obtained the standard deviation map inside the masked region. The mean of the standard deviation is the mean cell membrane fluctuation. Figure 25(a) shows a thickness map from the sequence. Note that the background outside the RBC is much more uniform than in the case of laser illumination imaging. Figure 25(b) shows the binary mask obtained from the average map and Fig. 25(c) shows the standard deviation map, which shows the membrane fluctuations with a mean value of 30.9 nm for this particular cell. The color bars in Figs. 25(a) and 25(c) show the cell thickness in micrometers and the membrane fluctuation in nanometers, respectively.

4.3b. QPI of Beating Cardiomyocyte Cell

Studying cardiomyocyte differentiation is important to heart disease research and drug discovery screening. For functional cardiomyocyte, one indication of differentiation is the beating of a cell or cell clumps. As the beating rate can be a few hertz, we need to have a fast QPI method to study the dynamics quantitatively. We have used our fast wDPM system to image dynamic cardiomyocyte beating at 2.5 Hz. Figure 26(a) shows a quantitative phase image

Figure 25

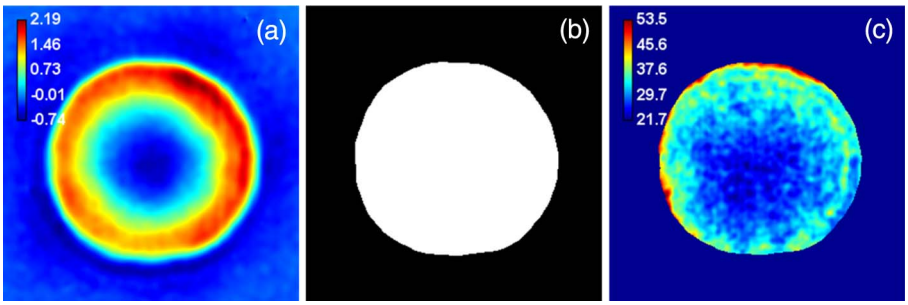

RBC membrane fluctuation measurement with wDPM. (a) RBC thickness map. (b) Generated binary mask. (c) Standard deviation map. Color bar in (a) shows thickness in micrometers and that in (c) shows standard deviation in nanometers. The mean of the standard deviation in the masked area is 30.9 nm.

of such a cardiomyocyte from the time-lapse sequence acquired at 50 Hz. The color bar shows the phase in radians. Figures 26(b) and 26(c) show line profiles of phase along lines AB and CD, respectively, in Fig. 26(a) at different times. The spikes are due to cell beating, and time difference between two spikes determines the beating period.

4.3c. Cell Growth Study

White-light DPM is built as an add-on module to a commercial bright-field microscope that is equipped with an incubator and heating stage for imaging live

Figure 26

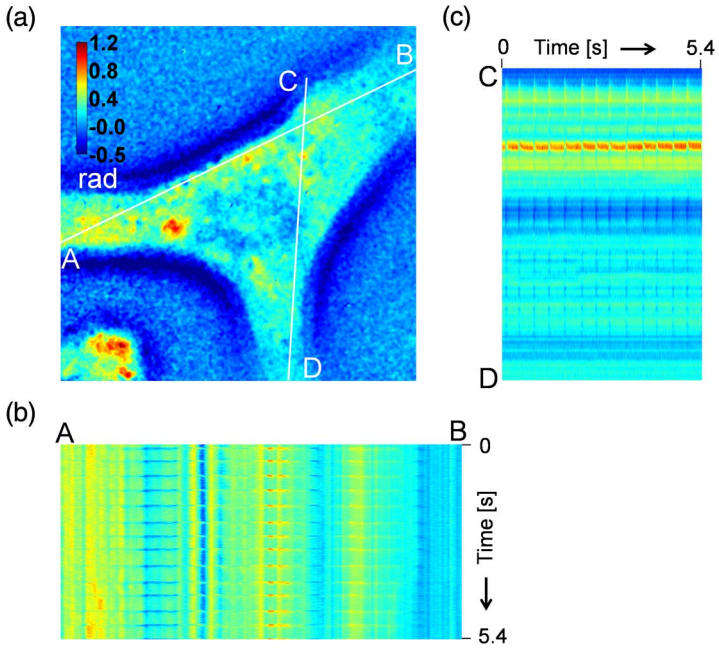

Beating cardiomyocyte imaging with wDPM. (a) Phase image. (b) Phase profile along line AB. (c) Phase profile along line CD. Color bar shows phase in radians.

Figure 27

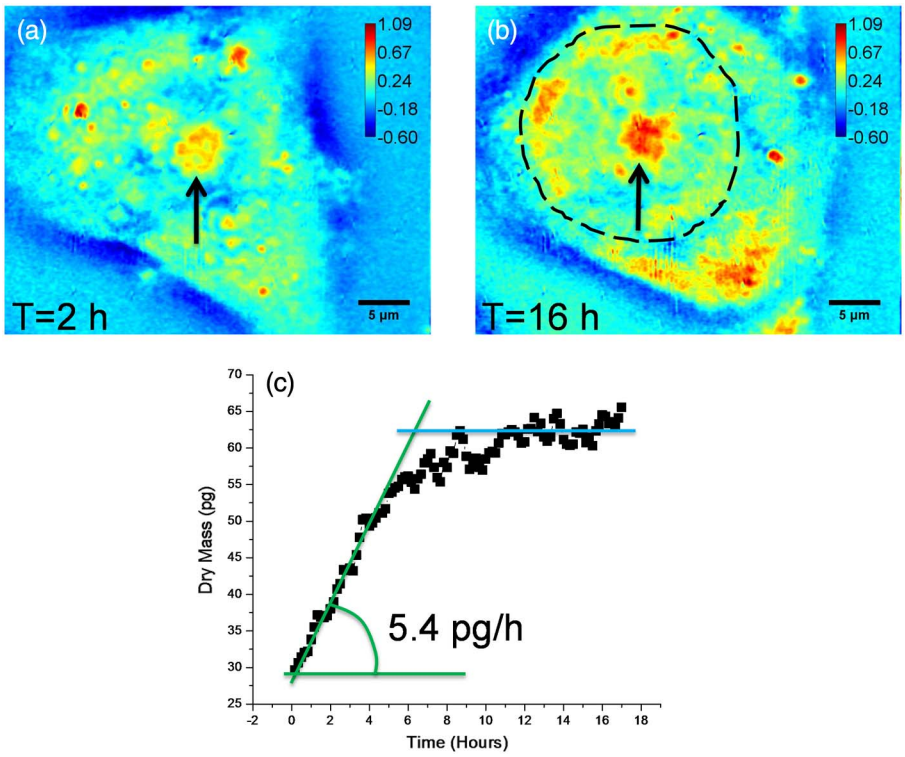

Cell growth measurement with wDPM. (a) and (b) Time-lapse quantitative phase images of an isolated HeLa cell at $T = 2$ h and $T = 16$ h. (c) Variation of dry mass with time for the HeLa cell during its growth. Color bars represent phase in radians. Adapted from [54].

cells up to several days. We have used a human cervical epithelial cell line, HeLa cells (ATCC, CCL-2), to quantify cell growth. Time-lapse wDPM images were acquired once every 10 min for 18 h. The dish was covered with a cover glass to reduce the effect of evaporation. Figures 27(a) and 27(b) show quantitative phase images of the cell at $T = 2$ h and $T = 16$ h, respectively, which reveals the cell structure (nucleolus is indicated by an arrow and nucleus is indicated by a dashed circle). Figure 27(c) shows the variation of total dry mass in picograms (pg) with time in hours, which clearly reveals the cell growth. This particular cell appears to be growing at a fast rate of 5.4 pg/h for the first 6 h, after which the growth slows and finally saturates slightly above the double mass level. Higher fluctuations in dry mass at later time points ($T > 6$ h) are due to cell fragments and debris floating in the culture medium, which adds noise to our measurement.

4.4. Spectroscopic DPM

4.4a. Existing Approaches

The phase delay measured in QPI is linearly related to the refractive index and thickness of the sample. For cells, this refractive index is proportional to concentration of proteins [108]. Several QPI methods have shown their ability to provide nanoscale, quantitative morphological analysis, as well as several novel clinically relevant parameters for RBCs at the single cell level [21,80,109–111].

However, since the optical phase shift is a function of both thickness and refractive index, more than one measurement is needed to decouple the thickness and refractive index of the cells. Existing approaches to solve this problem include measuring the phase shift with respect to two different media with different refractive indices or measuring quantitative phases at different light colors. The former approach requires the cells be kept in place as the media is changed and thus may not be well suited for clinical measurements [112,113]. Park *et al.* [114] developed spectroscopic phase microscopy (SPM), which is essentially DPM at different wavelengths using several BPFs with white-light illumination. Imaging the quantitative phase maps at different wavelengths helps differentiate among molecules. This instrument has many potential applications, one of which is quantifying isomeric shifts in Hb (oxy- and deoxy-Hb) when exposed to different oxygen pressures. Binding of oxygen to Hb proteins causes conformational changes that result in significant differences in dispersion. Thus, an SPM instrument may provide a valuable tool for the better understanding of oxygen transport by RBCs. Similarly, Fu *et al.* [115] developed a dual-wavelength quantitative phase microscope, also based on DPM, using two independent laser sources at different wavelengths. Further, quantitative phase spectroscopy (QPS) was recently proposed by using a supercontinuum laser and an acousto-optic tunable filter; it is capable of measuring the wavelength-dependent refractive index of microscopic volumes [116]. Quantitative phase images of semitransparent samples are recovered at each wavelength using off-axis interferometry and are processed to recover relative and absolute dispersion measurements.

4.4b. Spectroscopic DPM with White Light

One limitation of most of the above methods is that they require mechanical moving components in the system: switching of the filters [114], or filter wheel [106] or manual switching of the media [113]. Although the QPS method allows quantitative phase imaging at several wavelengths with high spectral resolution across the visible range, it requires an expensive supercontinuum laser light source and a tunable filter. In this section, we present a new method, *spectroscopic diffraction phase microscopy* (sDPM), that can measure quantitative cell-induced phase shifts at several wavelengths [117]. Spectroscopic DPM requires no moving parts in the system, and the spectroscopic measurement can be performed simply by changing PowerPoint slides projected on a projector SLM, which can be done automatically with full digital control. The sDPM method is demonstrated by measuring the dispersion of microsphere beads and hemoglobin-induced dispersion in RBCs.

The sDPM setup is similar to that of wDPM except for the filter mask projected on the SLM, as shown in Fig. 28. The key observation is that, because of the diffraction grating, different wavelengths are diffracted at different diffraction angles, and thus the 1st order is dispersed at the Fourier plane. Lens L2 then focuses the dispersed signal back to the same point in the image plane. Based on this observation, in order to select the wavelengths, we project a pinhole (a circular mask on the SLM) at different positions in the 1st order, as depicted in inset a in Fig. 28. Of course, the 0th order is not dispersed in wavelengths, i.e., it maintains a white color. The lens system L1–L2 forms a highly stable Mach–Zehnder interferometer. The filtered 1st order is used as the reference beam, and the 0th order is the imaging field. The two beams are interfered on a

Figure 28

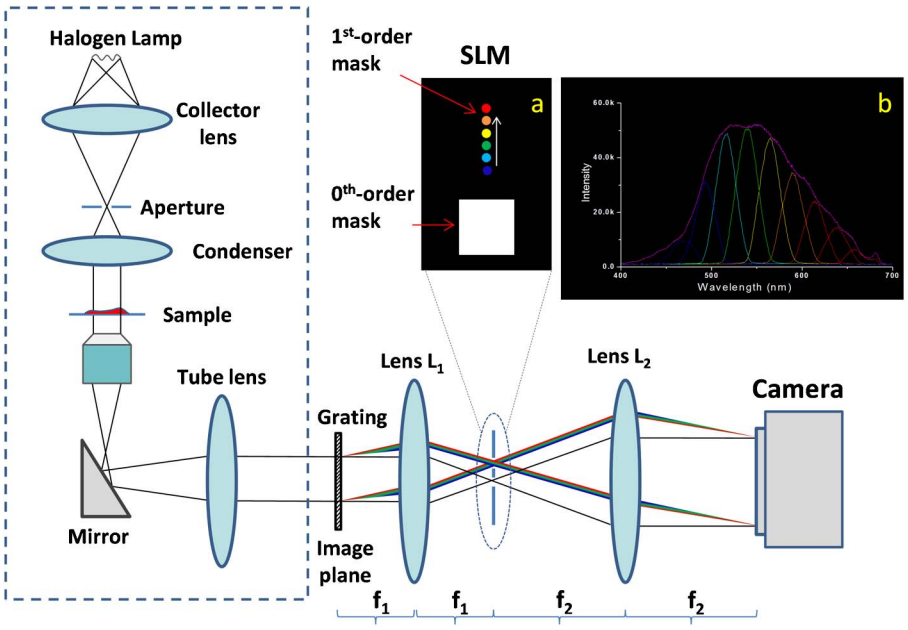

Experimental setup of sDPM. Inset a: scanning filters on the SLM. Inset b: first-order diffraction spectrum (outer envelope) and spectra at different wavelengths.

CCD camera at the image plane to generate a spatially modulated interference image. Note that the fringes observed are due to the interference between the light at the color selected by the pinhole and the white light of the 0th order. The contrast of the fringes is reduced because of the incomplete overlap in spectra, but is still more than sufficient to allow us to successfully reconstruct the phase images. For the experiments in this section, we used a bright-field objective (40×, 0.75 NA), and the diameter of the pinhole (0th order mask) at the Fourier plane is 200 μm. We used an Ocean Optics USB2000 + Fiber Optic Spectrometer to measure the spectrum of the 1st order. Inset b in Fig. 28 shows the whole spectrum (the pink outer envelope) and the spectra corresponding to different positions of the pinhole. The FWHM of each spectrum is 28 ± 1 nm. The mean wavelength of each spectrum is then used to calculate the expected phase shift corresponding to each pinhole position.

To test the system, we measured polystyrene microsphere beads immersed in Zeiss immersion oil. To calculate the expected phase shifts, we also took into account the dispersion of the immersion oil. Figure 29(a) shows the reconstructed phase maps of the 2.9 ± 0.14 μm polystyrene bead at four different wavelengths (565, 589, 613, and 640 nm) and the average phase values (red dashed curve) for ten polystyrene microspheres, with the error bar indicating standard deviation error. The measured dispersion agrees very well with the expected dispersion [80] shown by the blue solid curve. Next we demonstrate an important application of sDPM, by measuring the dispersion of RBCs. For RBCs, the phase shift in Eq. (2.3-1) can be rewritten as

$$\Delta\phi(x,y;\lambda) = k_0[\beta(\lambda)C(x,y) + \Delta n_{ws}(\lambda)]h(x,y), \tag{4.3-1}$$

where β is the *refractive increment* of protein in mL/g, C is the concentration in g/mL, and Δn_{ws} is the difference between the refractive index of water and that

Figure 29

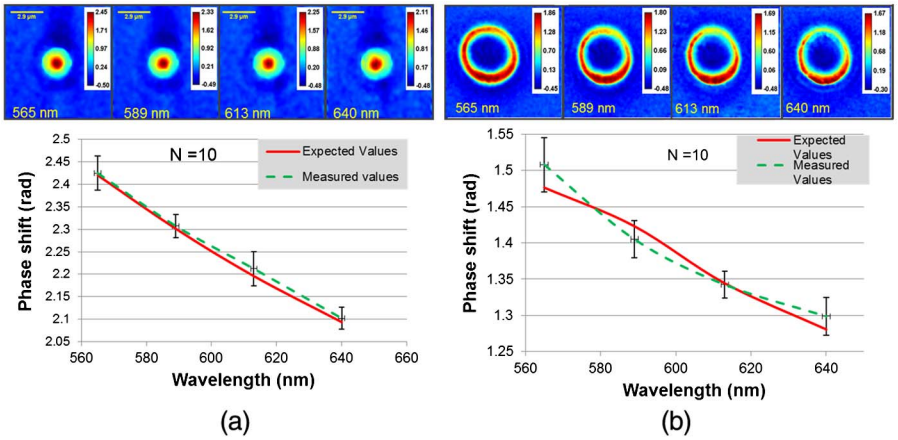

Reconstructed phase maps in radians at different wavelengths and dispersion curves of microbeads and red blood cells. (a) 3 μm beads in Zeiss immersion oil. (b) Red blood cell. Measured (dashed line) and expected (solid line) dispersion curves. The error bars indicate standard deviation ($N = 10$). Adapted from [117].

of the surrounding media. Figure 29(b) presents phase maps of an RBC at the same four different wavelengths and the dispersion curve associated with these measurements. We use $C = 32$ g/dL and data for the refractive increment β from the literature [118] to compute the expected phase shift of a 2 μm thick RBC. For the measured data, we normalized the phase values of each cell to the mean of the end points of the measured dispersion to remove the errors due to variations in RBC thickness values; different thicknesses shift this curve only vertically. Then the phase value at each wavelength was averaged over 10 cells.

In summary, by adding simple optics, we can convert a commercial microscope to a quantitative phase spectroscopy instrument, sDPM, capable of measuring quantitative phase maps at multiple wavelengths. This method has the advantage of using existing microscopes with minimal changes, and the selection of the wavelength can be done automatically with full digital control. This technique will be very useful for studying various blood disorders.

5. Real-Time DPM

We demonstrate a real time off-axis QPI system that is capable of reconstructing and displaying phase images in real time at 40 frames/s. This performance is achieved by combining high-speed single-shot off-axis diffraction phase microscopies with a reconstruction algorithm based on NVIDIA's CUDA parallel computing architecture. The developed software method can be used with both laser and white-light diffraction phase microscopies. For the demonstration in this section, we chose to use wDPM. As for the applications, we show, for the first time to our knowledge, real-time analysis of blood smears. While the slide is scanned throughout the FOV, the instrument analyzes and displays several blood parameters at the single cell level and in the end performs population statistics. Even though automatic blood analyzers, such as flow cytometers and impedance counters, have been proven to be effective tools for physicians and researchers,

they provide limited information on the detailed morphology of individual cells, and merely alert the operator to manually examine a blood smear by raising flags when abnormalities are detected. Our method provides the same information on RBCs as is provided by current automatic analyzers, while giving additional, currently unavailable parameters on the 2D and 3D morphology of individual RBCs.

5.1. Real-Time Phase Reconstruction Using Graphics Processing Units

As discussed earlier, the phase images can be reconstructed using Hilbert transform. However, the reconstructed phase images often have phase wrapping issues and a phase unwrapping process needs to be used to get the final phase images. There are two main types of phase unwrapping algorithm: path-following algorithms and the minimum-norm algorithms [119]. A classic path-following algorithm, Goldstein's algorithm, achieves the fastest performance; however, its implementation in sequential code is still slow and far from meeting real-time requirements. For example, Goldstein's algorithm implemented in C-code takes about 150 ms to unwrap a 1024×1024 pixels modulo-2π image from DPM [42], in addition to about 300 ms to extract the modulo-2π image from the raw DPM data.

In this section, we demonstrate real-time off-axis QPI by developing a phase reconstruction algorithm based on NVIDIA's CUDA programming model. In the CUDA programming model, graphics processing units (GPUs) are used as computation devices and operate as coprocessors to the central processing unit (CPU) [120]. These computation devices perform computationally intensive parts in parallel. Hundreds of processor cores operate together to process the same instruction but on different segments of the dataset in the application. Previous work on using GPUs for 2D phase unwrapping include Karasev *et al.* [121] and Mistry *et al.* [122]. The former implemented a weighted least-squares algorithm for interferometric synthetic aperture radar (IFSAR) data, and the latter implemented a minimum *Lp* norm phase unwrap algorithm for an optical quadrature microscopy system. Karasev *et al.* reported a 35× speed-up in weighted least-square 2D phase unwrapping, but it still takes 5.69 s to unwrap one 1024×1024 pixel image. In the latter work, it reportedly takes 2.8 s to unwrap one 640×480 pixel image.

Figure 30 illustrates a flow chart of the procedure to reconstruct the phase images from the interferograms. The phase extraction module performs the Hilbert transform, which is equivalent to the following steps: perform Fourier transform of the interferogram; shift the first-order peak to the center and filter everything else out; and then perform an inverse Fourier transform and arctangent operation. We chose the Goldstein algorithm for phase unwrapping since it is fast and performs well with our images. In this section, we present the implementation of the phase reconstruction algorithm on a GPU. To further utilize the GPU's power, we developed a program that can process multiple images simultaneously. This will be useful for streaming-type applications.

5.1a. Phase Extraction Module

This module to extract phase information from interferogram images involves Fourier transforms, point-wise matrix multiplications (for filtering), shifting of

Figure 30

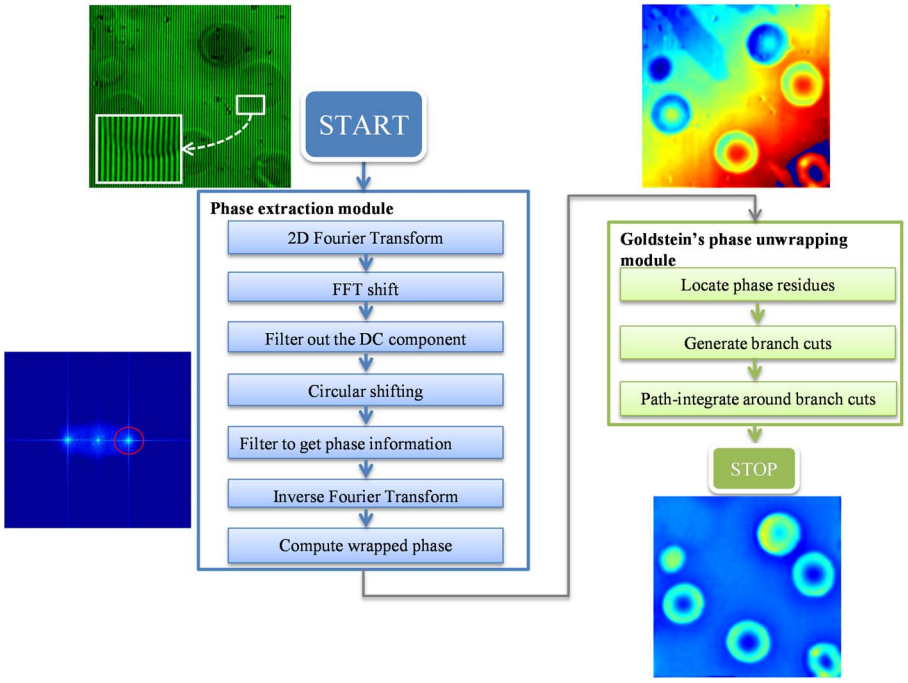

Phase reconstruction procedure of an off-axis quantitative phase imaging system.

matrix entries, and computing the argument of the complex number at each pixel of the image. For Fourier transforms, we use the CUFFT library developed by NVIDIA [123]. In the Fourier domain, the filtering part is simply point-wise matrix multiplication and the fast Fourier transform shifting, circular shifting, and the arctangent operation are all very straightforward for parallel implementation since there are no dependencies between data points. These operations are implemented using a thread-per-pixel model that assigns a thread to compute for each pixel of the image.

5.1b. CUDA-Based Phase Unwrapping Algorithm

The first step in the Goldstein algorithm, *residue identification*, is done on a pixel-by-pixel basis; each thread computes an integral over a closed four-pixel loop to decide whether the pixel at the top-left corner of the loop is a residue or not. This information is then stored in an array of byte type, called a bitflag array [51], to mark the pixel as a positive/negative residue. Next, the branch cut algorithm includes processes of enlarging and searching over a search box on the image to connect the residue to balance out the charge. This process requires knowledge about other residues it encounters during the search, such as whether it has been visited by other searches or it has already been connected to some other residues. Thus, this process is very difficult to parallelize. One can implement this process sequentially in the host code, but this requires data copies between the GPU device's memory and the host memory, which introduces a significant time delay. To avoid this back-and-forth copying, for each image we use one thread to perform this step. Furthermore, instead of scanning over the whole image to search for residues, as in the original Goldstein algorithm, we perform the search on the residue lists stored in the residue identification step.

This way of implementation may be computationally intensive if the number of residues is large; however, for our system, the number of residues is often small, and this implementation performs much better than the host code one.

The last step of the Goldstein algorithm is also difficult to parallelize because of data dependency between pixels; i.e., unwrapping a pixel requires that one of its neighbors has already been unwrapped. The most direct way to do this in CUDA is that each thread performs the unwrapping function for each pixel if one of its neighbors is marked as unwrapped. However, thread execution is asynchronous, and only threads in the same block can cooperate; and the maximum number of threads per block supported by existing devices is 1024, limiting us to very small images. Furthermore, since each pixel is repeatedly read by its neighbors, this process may become computationally intensive due to repeated memory reading. Instead, we choose to assign each thread to be responsible for unwrapping one row or column of the image and change the direction of scanning. Also, in each scan, we check only the previous pixel in the scanning direction to see whether it is flagged as unwrapped. In each scanning, the process is stopped if the unwrapped path meets a branch cut pixel, and the remaining wrapped pixels will be unwrapped in later scans in other direction or iterations. The scanning continues until all the pixels in isolated regions are unwrapped. For each isolated

Figure 31

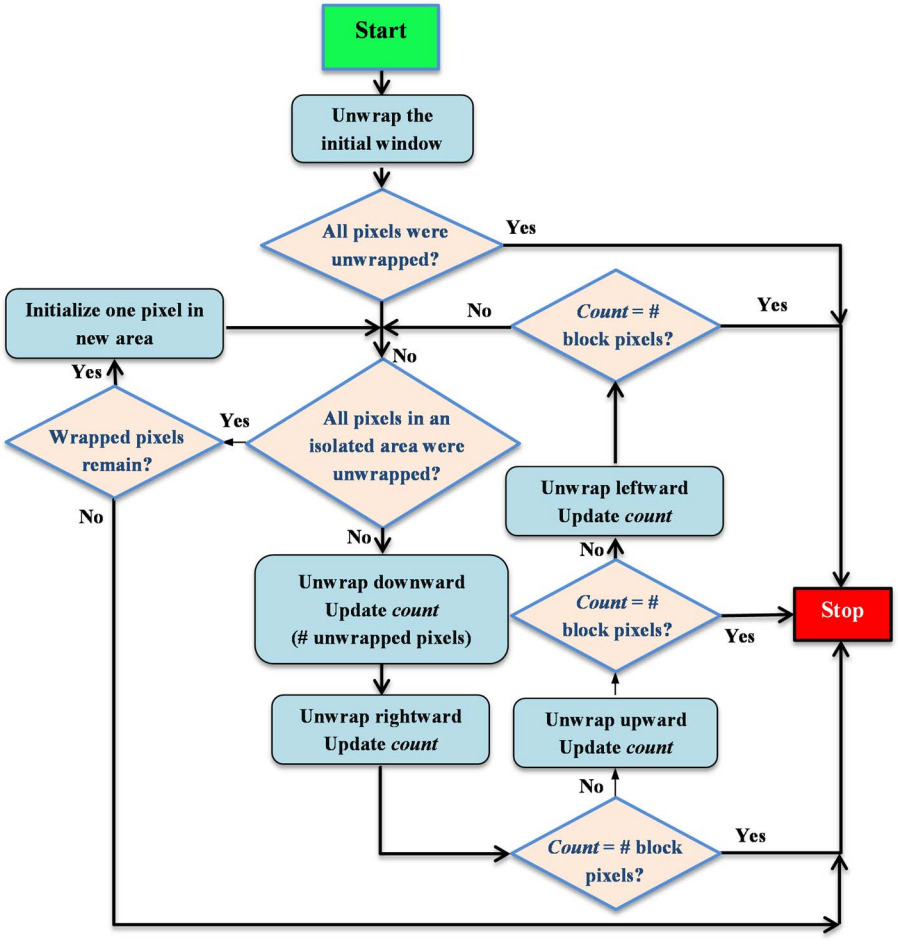

Flow chart of the unwrapping step.

Table 2. CUDA Implementation versus C-Based Sequential Implementation

Image Size	CPU/GPU	Phase Extraction (ms)	Residue Identification (ms)	Branch Cut Placement (ms)	Unwrap (ms)	Total (ms)
1024 × 1024	CPU	317.42	43.42	6.74	89.32	460.7
1 frame	GPU	5.05	0.58	1.125	10.014	24.55
	Speedup factor	**62.86**	**74.19**	**5.99**	**8.92**	**18.77**
1024 × 1024	CPU	3174.2	434.2	67.4	893.2	4607.4
10 frames	GPU	40.486	5.55	1.128	45.285	111.1
	Speedup factor	**78.4**	**78.19**	**59.71**	**19.72**	**41.47**
512 × 512 1	CPU	71	11	5	16	105
frame	GPU	2.18	0.2	0.02	1.87	8
	Speedup factor	**32.61**	**55.84**	**250**	**8.55**	**13.13**
512 × 512	CPU	710	110	50	160	1050
10 frames	GPU	11.57	1.4	0.02	6.722	26
	Speedup factor	**61.37**	**78.57**	**2500**	**23.8**	**40.38**

region, we first initialize a pixel in the region and repeat the above process. This initial pixel was chosen in the scanning process of the previous isolated region. Figure 31 presents the flow chart of this last step.

5.1c. Performance Results

We tested the algorithm on a Windows machine with Intel Core i5 CPU with clock rate of 3.2 GHz and 8 GB RAM memory. We use NVIDIA GeForce GTX 470M GPU that supports CUDA programming.

Table 2 compares the performances of the developed parallel algorithm with the sequential C-code-based implementation [119]. The results shown were averaged over 20 images for each image size. In the case of processing multiple image frames simultaneously, for the sequential C-code program the run time simply scales linearly with the number of frames. For GPU implementation, the total run time includes time for the memory copy of interferogram from host to device and also a memory copy of the output unwrapped image from device to host. Clearly, the GPU implementation performs much faster than the sequential one.

5.2. Applications

In clinical settings, existing technologies used for blood testing, such as impedance counters and flow cytometers, are often accurate and offer high throughput. However, they are expensive and provide only limited information about the RBCs, such as the mean corpuscular volume (MCV) and hemoglobin concentration. Based on these parameters, the instrument flags abnormalities, and, usually, a trained physician is required to visually assesses the *stained* blood smears through the light microscope for further evaluation on the detailed morphology of the RBCs. The process of staining requires dedicated infrastructure, i.e., specialized instruments, dyes, and trained personnel [124]. These requirements have prevented blood testing from becoming universally available, especially in economically challenged countries and rural areas. To address this

problem, researchers have developed several solutions to decrease the cost of the imaging instruments by utilizing existing and popular commercial devices, such as cell phone cameras, and converting them into disposable accessories [125,126]. However, so far, these instruments provide only *qualitative* information and require further analysis by trained staff. Of course, the data can be transmitted for remote diagnosis, a principle known as *telepathology* [127]; however, the output data usually is a large volume of images, and transferring a large dataset may be difficult in economically challenged areas.

Instead of focusing on reducing the instrument cost, we developed a highly sensitive blood testing instrument that operates in real time and outputs data that contains *quantitative* analysis, providing rich diagnostic information [128]. The measured phase image provides nanometer-scale information about the RBC profile, which translates into highly sensitive measurement of the volume and morphology. Thousands of images are then analyzed, and the outputs are in the form of arrays of numbers that characterize the morphology and dynamics of RBCs. Therefore, the output data size is small (kilobytes of memory) and can be easily transmitted for remote diagnosis. We combine the single-shot highly sensitive imaging method (wDPM) with parallel image processing algorithms to extract morphological parameters at the single cell level from the entire FOV (1 megapixel) in less than 25 ms and to analyze an entire blood smear in a few minutes. Thus, since the blood necessary for this test can be obtained via a simple finger prick, we envision that our instrument can operate in economically challenging areas where access to clinical settings is limited.

Figure 32 shows the overall architecture of our system. At the beginning of each measurement, a background subtraction is necessary to remove the effects of inherent dust and aberrations along the optical path. Since we want to have 2D and 3D morphological information on each single cell, the phase

Figure 32

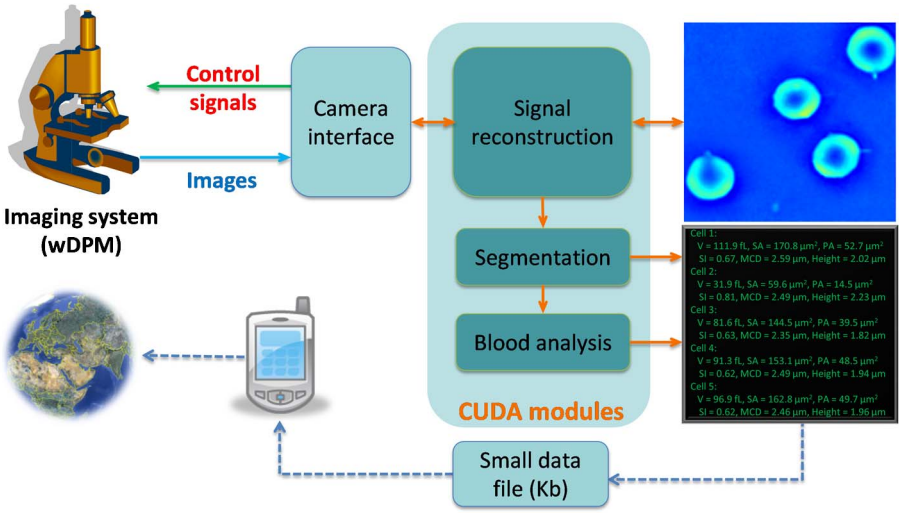

Overview of the blood-testing instrument. The white-light diffraction phase microscope is used as the imaging system. Different CUDA modules perform phase reconstruction and image analysis to calculate several morphological parameters of individual RBCs. The output information is in the form of arrays of numbers and can be easily transmitted for remote diagnosis.

reconstruction algorithm is followed by cell *segmentation and analysis*. This module is responsible for isolating and labeling each individual cell in the FOV and then calculating various morphological parameters associated with each cell while the blood smear is scanned through the FOV.

5.2a. Single Cell Parameters Computed in Real Time

First, the projected area (PA) parameter can be easily obtained by multiplying the number of pixels of each cell by the camera pixel area and dividing by the magnification of the imaging system. The PA then can be used to calculate the *equivalent circular diameter*, assuming that the projected area of a RBC is a circular disk. As we know, the measured phase shift is proportional to the thickness and refractive index of the cells. If we know the refractive index of RBCs, the phase map $\phi(x,y)$ can be converted to a height map $h(x,y)$ as $h(x,y) = \lambda\phi(x,y)/2\pi\Delta n$, where λ is the wavelength of the light source and $\Delta n = n_c - n_0$ is the refractive index difference between RBCs and the surrounding medium. Once the height information is retrieved, the *volume* of each cell is calculated by integrating the height map over the PA as $V = \iint h(x,y)\mathrm{d}x\mathrm{d}y$. To calculate the *surface area*, we use Monge parameterization [129], where the contribution of each pixel element dA can be calculated as $dA = P_{\text{area}}(1 + h_x^2 + h_y^2)^{1/2}$, where P_{area} is the area of 1 pixel, and h_x and h_y are the gradients along the x and y directions, respectively. The surface area of each cell is then the sum of all the area elements dA of all the pixels within the cell boundary and the PA, as the cell lays flat on the coverslip. The volume and the surface area determine the shape of the cell; from these two parameters, we can calculate several morphological parameters characterizing the RBCs, such as sphericity and minimum cylindrical diameter (MCD), determined as important parameters by Canham and Burton [130]. The sphericity index is calculated as $\psi = 4.84\ \mathrm{V}^{2/3}/\mathrm{SA}$. The MCD predicts the smallest capillary diameter that a RBC with that given shape can squeeze through and, thus, is clinically significant. Furthermore, we are able to calculate many other independent parameters [106], including: perimeter, circular diameter, eccentricity, minimum, maximum, and mean thickness, circularity, integrated density, kurtosis, skewness, and variance. Therefore, our method provides rich and detailed information at the single cell level and at the population level with several thousands of cells per patient. This capability allows us to come up with several analysis tools and look at different sets of parameters and their relations to study and characterize abnormal cells and diseases that would otherwise be difficult or impossible to detect in an impedance counter or manually in a smear.

5.2b. Cell Segmentation and Connected Component Labeling

To calculate single cell parameters, we have to be able to isolate and label different cells in the FOV. To do that, for each image, we will have a label map initiated with all zeroes at all pixel positions, apply a threshold to the reconstructed phase map to separate objects of interest from the background, update the label map, and label each non-background pixel with a label equal to the pixel index in the image; this label is regarded as its initial reference. At the same time, we calculate the volume and surface area contributions, and assign a pixel count (equal to 1, to be used to calculate PA, average height, and other parameters later) at each and every non-background pixel simultaneously.

To calculate the parameters for each cell, we need to group all the pixels in the same cell together and label them using the same label value. This is called the connected component labeling problem, and numerous approaches for connected component labeling have been introduced [131–133]. Recently, some researchers developed parallel algorithms of graph component labeling with GPUs [134,135]. We adapted the *label equivalent* algorithm [135] to develop our image analysis tool. The result gives a map with background pixels of value 0 and groups of pixels with different values for different groups; all pixels in the same connected region should have the same label values. Finally, different parameters are calculated for each cell and displayed as shown in Fig. 5. Using our current GPU graphics card (GTX570), we can acquire images and perform all the processing of up to 40 megapixel-size image frames/second, and, of course, this rate can be increased with more powerful GPU cards.

5.2c. Results

We tested the program on a Windows machine with Intel Core i5 CPU with clock rate of 3.2 GHz and 8 GB RAM memory. We use NVIDIA GeForce GTX 570M GPU, which supports CUDA programming. We performed a clinical study on blood samples from patients with normal blood and with macrocytic and microcytic anemia. The blood samples were provided by Provena Covenant Medical Central laboratory. After the volume calibration measurement on the blood sample of another normal patient, we measured 6181 RBCs of the normal patient, 8442 RBCs of the patient with microcytosis anemia disease, and 4535 RBCs of the patient with macrocytosis disease. Figure 33(a) shows the distributions of RBCs volumes for the three patients with the MCV values for the normal, microcytic, and macrocytic patients being 92.5, 67.4, and 125.6 femtoliters, respectively. The results agree very well with the data acquired by the clinical impedance counter, which are 92.2, 64.4, and 121.8 femtoliters, respectively. The inset in Fig. 6(a) shows this agreement between our measured data and the data from the clinical impedance counter. Furthermore, the widths of the

Figure 33

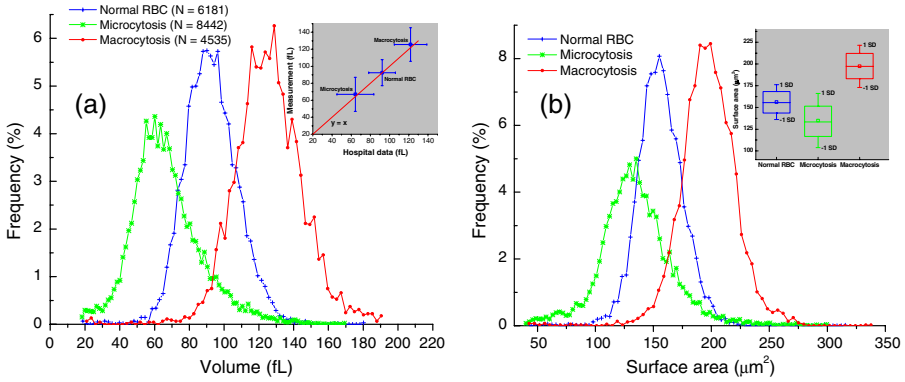

Morphological parameter distribution of RBCs of a healthy patient ($N = 6181$ cells) and patients with microcytic ($N = 8442$ cells) and macrocytic ($N = 4535$ cells) anemias. (a) Cell volume and comparison of measured data versus hospital data. (b) RBC surface area distribution of the three patients. Adapted from Pham *et al.*, "Real time blood testing using quantitative phase imaging," PLOS One **8**, e55676 (2013) [128].

Figure 34

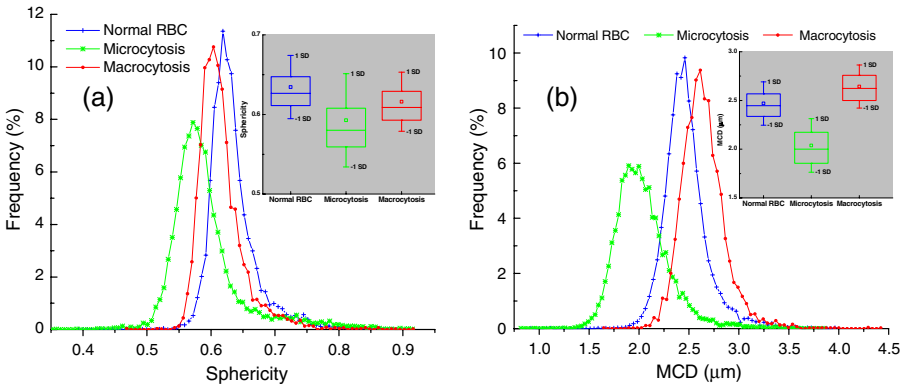

Examples of output distributions of other morphological parameters. (a) Sphericity index. (b) MCD. Adapted from Pham *et al.*, "Real time blood testing using quantitative phase imaging," PLOS One **8**, e55676 (2013) [128].

red blood cell distribution (RDW) curves also show great agreement between our measured data and that from the Beckman–Coulter machine. This RDW value is also an important diagnostic parameter. An elevated RDW (red blood cells of unequal sizes) is known as *anisocytosis*. Specifically, the RDW values for normal, microcytic, and macrocytic patients are 16.5%, 30.1%, and 15.6%, respectively, which agree very well with the data from the clinical analyzers (15%, 29.7%, and 13.9%, respectively). Figure 33(b) shows, as expected, that the cell surface area is increasing from microcytic, to normal, to macrocytic cells. The inset in Fig. 33(b) shows statistical information at population level of each patient with a range to indicate standard deviation and boxes to illustrate interquartile range.

In addition to parameters that the automatic analyzers provide, our system is able to provide several more 2D and 3D morphological parameters in great detail. Figures 34(a) and 34(b) show some other example distributions of the sphericity index and MCD, respectively, with the insets showing the statistical information for each patient. Current automated analyzers cannot provide these parameters. Thus, a pathologist has to manually examine a smear to confirm diagnosis of spherocytosis if the results from automatic analyzers raise a warning flag of that possibility. Our system provides this diagnosis in great detail using the sphericity index for each and every single cell.

6. Summary and Discussion

DPM has enabled numerous applications in both materials and life sciences. DPM's off-axis geometry allows single-shot measurements and the study of rapid phenomena. More importantly, DPM is a common-path technique, which ensures phase stability against noise and, thus, high temporal phase sensitivity. Because it uses a diffraction grating at the image plane, specific sampling conditions must be satisfied to preserve the diffraction-limited resolution. Section 2 establishes quantitative constraints on the grating period versus diffraction spot size at the image plane, as well as pixel size versus grating period at the camera plane.

Originally, DPM was developed with laser illumination (Section 3), but later the operation principle was extended to white light (Section 4). Laser illumination has a clear advantage in terms of brightness. For example, laser light can be coupled into a single-mode fiber and further collimated, which can easily ensure the high spatial coherence necessary for accurate phase measurements. When using white light, on the other hand, speckles are significantly averaged, improving the spatial phase sensitivity. Furthermore, this illumination mode can be achieved by using existing microscopes without changing their typical illumination. Thus, common halogen lamps can be used, provided the condenser aperture is reduced to ensure spatial coherence. However, these sources are spatially extended, and, thus, achieving high spatial coherence can be achieved only with significant loss in power.

We described laser DPM in both transmission and reflection geometries. The transillumination reveals details about transparent structures, such as unstained cells and thin slices of tissues. More recently, the DPM principle has been extended to epi-illumination to study materials that are opaque in the visible range of the spectrum, including silicon wafers and semiconductor structures. Monitoring in real-time topography using manufacturing processes is an exciting new field of application for DPM and QPI in general.

Finally, Section 5 describes how recent advances in computing, especially using GPUs, allow performance of previously impossible tasks, such as real-time quantitative phase imaging of dynamic samples. It is now possible to analyze images and extract quantitative information in real time. This trend is likely to continue, eliminating one day the need to save the images in the first place. Transforming the microscope into an instrument that outputs information and not just images is the ultimate goal and a concept that perhaps Gabor envisioned 70 years ago.

References

1. F. Zernike, "Phase contrast, a new method for the microscopic observation of transparent objects, Part 1," Physica **9**, 686–698 (1942).
2. F. Zernike, "Phase contrast, a new method for the microscopic observation of transparent objects, Part 2," Physica **9**, 974–986 (1942).
3. D. Gabor, "A new microscopic principle," Nature **161**, 777–778 (1948).
4. D. Gabor, "Theory of communication," J. Inst. Electr. Eng. **93**, 429–457 (1946).
5. A. Lohmann, "Optische Einseitenbandübertragung angewandt auf das Gabor-Mikroskop," Opt. Acta **3**, 97–99 (1956).
6. E. Leith and J. Upatnieks, "Reconstructed wavefronts and communication theory," J. Opt. Soc. Am. **52**, 1123–1128 (1962).
7. J. W. Goodman and R. W. Lawrence, "Digital image formation from electronically detected holograms," Appl. Phys. Lett. **11**, 77–79 (1967).
8. M. Takeda, H. Ina, and S. Kobayashi, "Fourier-transform method of fringe-pattern analysis for computer-based topography and interferometry," J. Opt. Soc. Am. **72**, 156–160 (1982).
9. U. Schnars and W. Juptner, "Direct recording of holograms by a CCD target and numerical reconstruction," Appl. Opt. **33**, 179–181 (1994).

10. I. Yamaguchi and T. Zhang, "Phase-shifting digital holography," Opt. Lett. **22**, 1268–1270 (1997).
11. E. Cuche, F. Bevilacqua, and C. Depeursinge, "Digital holography for quantitative phase-contrast imaging," Opt. Lett. **24**, 291–293 (1999).
12. D. Carl, B. Kemper, G. Wernicke, and G. von Bally, "Parameter-optimized digital holographic microscope for high-resolution living-cell analysis," Appl. Opt. **43**, 6536–6544 (2004).
13. D. C. B. Kemper, J. Schnekenburger, M. Schäfer, W. Domschke, G. von Bally, I. Bredebusch, and D. Carl, "Investigation of living pancreas tumor cells by digital holographic microscopy," J. Biomed. Opt. **11**, 034005 (2006).
14. M. Paturzo, F. Merola, S. Grilli, S. De Nicola, A. Finizio, and P. Ferraro, "Super-resolution in digital holography by a two-dimensional dynamic phase grating," Opt. Express **16**, 17107–17118 (2008).
15. L. Miccio, A. Finizio, R. Puglisi, D. Balduzzi, A. Galli, and P. Ferraro, "Dynamic DIC by digital holography microscopy for enhancing phase-contrast visualization," Biomed. Opt. Express **2**, 331–344 (2011).
16. C. J. Mann, L. F. Yu, C. M. Lo, and M. K. Kim, "High-resolution quantitative phase-contrast microscopy by digital holography," Opt. Express **13**, 8693–8698 (2005).
17. A. Khmaladze, M. Kim, and C. M. Lo, "Phase imaging of cells by simultaneous dual-wavelength reflection digital holography," Opt. Express **16**, 10900–10911 (2008).
18. M. K. Kim, *Digital Holographic Microscopy: Principles, Techniques, and Applications* (Springer, 2011).
19. K. J. Chalut, W. J. Brown, and A. Wax, "Quantitative phase microscopy with asynchronous digital holography," Opt. Express **15**, 3047–3052 (2007).
20. N. T. Shaked, Y. Z. Zhu, M. T. Rinehart, and A. Wax, "Two-step-only phase-shifting interferometry with optimized detector bandwidth for microscopy of live cells," Opt. Express **17**, 15585–15591 (2009).
21. N. T. Shaked, L. L. Satterwhite, M. J. Telen, G. A. Truskey, and A. Wax, "Quantitative microscopy and nanoscopy of sickle red blood cells performed by wide field digital interferometry," J. Biomed. Opt. **16**, 030506 (2011).
22. L. Xu, X. Y. Peng, Z. X. Guo, J. M. Miao, and A. Asundi, "Imaging analysis of digital holography," Opt. Express **13**, 2444–2452 (2005).
23. W. J. Qu, Y. J. Yu, C. O. Choo, and A. Asundi, "Digital holographic microscopy with physical phase compensation," Opt. Lett. **34**, 1276–1278 (2009).
24. P. W. M. Tsang, K. W. K. Cheung, T. Kim, Y. S. Kim, and T. C. Poon, "Fast reconstruction of sectional images in digital holography," Opt. Lett. **36**, 2650–2652 (2011).
25. S. S. Kou and C. J. R. Sheppard, "Imaging in digital holographic microscopy," Opt. Express **15**, 13640–13648 (2007).
26. L. F. Yu, S. Mohanty, J. Zhang, S. Genc, M. K. Kim, M. W. Berns, and Z. P. Chen, "Digital holographic microscopy for quantitative cell dynamic evaluation during laser microsurgery," Opt. Express **17**, 12031–12038 (2009).
27. A. Anand, V. K. Chhaniwal, and B. Javidi, "Real-time digital holographic microscopy for phase contrast 3D imaging of dynamic phenomena," J. Disp. Technol. **6**, 500–505 (2010).
28. G. Nehmetallah and P. P. Banerjee, "Applications of digital and analog holography in three-dimensional imaging," Adv. Opt. Photon. **4**, 472–553 (2012).

29. K. J. Gåsvik, *Optical Metrology* (Wiley, 2002).
30. H. G. Davies and M. H. F. Wilkins, "Interference microscopy and mass determination," Nature **169**, 541 (1952).
31. R. Barer, "Interference microscopy and mass determination," Nature **169**, 366–367 (1952).
32. G. Popescu, *Quantitative Phase Imaging of Cells and Tissues* (McGraw-Hill, 2011).
33. C. L. Curl, C. J. Bellair, P. J. Harris, B. E. Allman, A. Roberts, K. A. Nugent, and L. M. D. Delbridge, "Quantitative phase microscopy: a new tool for investigating the structure and function of unstained live cells," Clin. Exp. Pharmacol. Physiol. **31**, 896–901 (2004).
34. A. Barty, K. A. Nugent, D. Paganin, and A. Roberts, "Quantitative optical phase microscopy," Opt. Lett. **23**, 817–819 (1998).
35. F. Dubois, L. Joannes, and J. C. Legros, "Improved three-dimensional imaging with a digital holography microscope with a source of partial spatial coherence," Appl. Opt. **38**, 7085–7094 (1999).
36. F. Charrière, A. Marian, F. Montfort, J. Kuehn, T. Colomb, E. Cuche, P. Marquet, and C. Depeursinge, "Cell refractive index tomography by digital holographic microscopy," Opt. Lett. **31**, 178–180 (2006).
37. P. Marquet, B. Rappaz, P. J. Magistretti, E. Cuche, Y. Emery, T. Colomb, and C. Depeursinge, "Digital holographic microscopy: a noninvasive contrast imaging technique allowing quantitative visualization of living cells with subwavelength axial accuracy," Opt. Lett. **30**, 468–470 (2005).
38. C. H. Yang, A. Wax, I. Georgakoudi, E. B. Hanlon, K. Badizadegan, R. R. Dasari, and M. S. Feld, "Interferometric phase-dispersion microscopy," Opt. Lett. **25**, 1526–1528 (2000).
39. C. Yang, A. Wax, M. S. Hahn, K. Badizadegan, R. R. Dasari, and M. S. Feld, "Phase-referenced interferometer with subwavelength and subhertz sensitivity applied. to the study of cell membrane dynamics," Opt. Lett. **26**, 1271–1273 (2001).
40. G. Popescu, L. P. Deflores, J. C. Vaughan, K. Badizadegan, H. Iwai, R. R. Dasari, and M. S. Feld, "Fourier phase microscopy for investigation of biological structures and dynamics," Opt. Lett. **29**, 2503–2505 (2004).
41. T. Ikeda, G. Popescu, R. R. Dasari, and M. S. Feld, "Hilbert phase microscopy for investigating fast dynamics in transparent systems," Opt. Lett. **30**, 1165–1168 (2005).
42. G. Popescu, T. Ikeda, R. R. Dasari, and M. S. Feld, "Diffraction phase microscopy for quantifying cell structure and dynamics," Opt. Lett. **31**, 775–777 (2006).
43. S. S. Kou, L. Waller, G. Barbastathis, and C. J. R. Sheppard, "Transport-of-intensity approach to differential interference contrast (TI-DIC) microscopy for quantitative phase imaging," Opt. Lett. **35**, 447–449 (2010).
44. B. Bhaduri, K. Tangella, and G. Popescu, "Fourier phase microscopy with white light," Biomed. Opt. Express **4**, 1434–1441 (2013).
45. K. Lee, K. Kim, J. Jung, J. Heo, S. Cho, S. Lee, G. Chang, Y. Jo, H. Park, and Y. Park, "Quantitative phase imaging techniques for the study of cell pathophysiology: from principles to applications," Sensors **13**, 4170–4191 (2013).
46. T. Kim, R. Zhou, M. Mir, D. S. Babacan, S. P. Carney, L. L. Goddard, and G. Popescu, "White light diffraction tomography of unlabeled live cells," Nat. Photonics **8**, 256–263 (2014).

47. E. Abbe, "Beiträge zur Theorie des Mikroskops und der mikroskopischen Wahrnehmung," Arch. Mikrosk. Anat. **9**, 413–468 (1873).
48. B. E. A. Saleh and M. C. Teich, *Fundamentals of Photonics* (Wiley, 2013).
49. H. V. Pham, C. Edwards, L. L. Goddard, and G. Popescu, "Fast phase reconstruction in white light diffraction phase microscopy," Appl. Opt. **52**, A97–A101 (2013).
50. C. Edwards, A. Arbabi, G. Popescu, and L. L. Goddard, "Optically monitoring and controlling nanoscale topography during semiconductor etching," Light Sci. Appl. **1**, e30 (2012).
51. H. Pham, H. Ding, N. Sobh, M. Do, S. Patel, and G. Popescu, "Off-axis quantitative phase imaging processing using CUDA: toward real-time applications," Biomed. Opt. Express **2**, 1781–1793 (2011).
52. B. Bhaduri and G. Popescu, "Derivative method for phase retrieval in off-axis quantitative phase imaging," Opt. Lett. **37**, 1868–1870 (2012).
53. G. Popescu, T. Ikeda, K. Goda, C. A. Best-Popescu, M. Laposata, S. Manley, R. R. Dasari, K. Badizadegan, and M. S. Feld, "Optical measurement of cell membrane tension," Phys. Rev. Lett. **97**, 218101 (2006).
54. B. Bhaduri, H. Pham, M. Mir, and G. Popescu, "Diffraction phase microscopy with white light," Opt. Lett. **37**, 1094–1096 (2012).
55. N. Mohandas and P. G. Gallagher, "Red cell membrane: past, present, and future," Blood **112**, 3939–3948 (2008).
56. R. Cotran, V. Kumar, T. Collins, and S. Robbins, *Robbins Pathologic Basis of Disease* (Saunders, 2004).
57. H. Engelhardt, H. Gaub, and E. Sackmann, "Viscoelastic properties of erythrocyte membranes in high-frequency electric fields," Nature **307**, 378–380 (1984).
58. M. P. Sheetz, M. Schindler, and D. E. Koppel, "Lateral mobility of integral membrane proteins is increased in spherocytic erythrocytes," Nature **285**, 510–512 (1980).
59. D. E. Discher, N. Mohandas, and E. A. Evans, "Molecular maps of red cell deformation: hidden elasticity and in situ connectivity," Science **266**, 1032–1035 (1994).
60. C. P. Johnson, H. Y. Tang, C. Carag, D. W. Speicher, and D. E. Discher, "Forced unfolding of proteins within cells," Science **317**, 663–666 (2007).
61. C. F. Schmidt, K. Svoboda, N. Lei, I. B. Petsche, L. E. Berman, C. R. Safinya, and G. S. Grest, "Existence of a flat phase in red cell membrane skeletons," Science **259**, 952–955 (1993).
62. J. D. Wan, W. D. Ristenpart, and H. A. Stone, "Dynamics of shear-induced ATP release from red blood cells," Proc. Natl. Acad. Sci. USA **105**, 16432–16437 (2008).
63. Y. Cui and C. Bustamante, "Pulling a single chromatin fiber reveals the forces that maintain its higher-order structure," Proc. Natl. Acad. Sci. USA **97**, 127–132 (2000).
64. T. R. Hinds and F. F. Vincenzi, "Evidence for a calmodulin-activated Ca^{2+} pump ATPase in dog erythrocytes," Proc. Soc. Exp. Biol. Med. **181**, 542–549 (1986).
65. M. Schindler, D. E. Koppel, and M. P. Sheetz, "Modulation of membrane protein lateral mobility by polyphosphates and polyamines," Proc. Natl. Acad. Sci. USA **77**, 1457–1461 (1980).
66. G. Bao and S. Suresh, "Cell and molecular mechanics of biological materials," Nat. Mater. **2**, 715–725 (2003).

67. B. Bain, *A Beginner's Guide to Blood Cells* (Blackwell, 2004).
68. J. B. Fournier, D. Lacoste, and E. Rapha, "Fluctuation spectrum of fluid membranes coupled to an elastic meshwork: jump of the effective surface tension at the mesh size," Phys. Rev. Lett. **92**, 18102 (2004).
69. M. Puig-de-Morales-Marinkovic, K. T. Turner, J. P. Butler, J. J. Fredberg, and S. Suresh, "Viscoelasticity of the human red blood cell," Am. J. Physiol. Cell Physiol. **293**, C597–C605 (2007).
70. E. Browicz, "Further observation of motion phenomena on red blood cells in pathological states," Zentralbl. Med. Wiss. **28**, 625–627 (1890).
71. N. Gov, A. G. Zilman, and S. Safran, "Cytoskeleton confinement and tension of red blood cell membranes," Phys. Rev. Lett. **90**, 228101 (2003).
72. A. Zilker, M. Ziegler, and E. Sackmann, "Spectral-analysis of erythrocyte flickering in the 0.3–4-μm^{-1} regime by microinterferometry combined with fast image-processing," Phys. Rev. A **46**, 7998–8001 (1992).
73. S. Tuvia, S. Levin, A. Bitler, and R. Korenstein, "Mechanical fluctuations of the membrane-skeleton are dependent on F-actin ATPase in human erythrocytes," J. Cell Biol. **141**, 1551–1561 (1998).
74. N. S. Gov and S. A. Safran, "Red blood cell membrane fluctuations and shape controlled by ATP-induced cytoskeletal defects," Biophys. J. **88**, 1859–1874 (2005).
75. C. L. L. Lawrence, N. Gov, and F. L. H. Brown, "Nonequilibrium membrane fluctuations driven by active proteins," J. Chem. Phys. **124**, 074903 (2006).
76. J. Li, M. Dao, C. T. Lim, and S. Suresh, "Spectrin-level modeling of the cytoskeleton and optical tweezers stretching of the erythrocyte," Biophys. J. **88**, 3707–3719 (2005).
77. F. Brochard and J. F. Lennon, "Frequency spectrum of the flicker phenomenon in erythrocytes," J. Phys. **36**, 1035–1047 (1975).
78. Y. Kaizuka and J. T. Groves, "Hydrodynamic damping of membrane thermal fluctuations near surfaces imaged by fluorescence interference microscopy," Phys. Rev. Lett. **96**, 118101 (2006).
79. A. Zilker, H. Engelhardt, and E. Sackmann, "Dynamic reflection interference contrast (RIC-) microscopy—a new method to study surface excitations of cells and to measure membrane bending elastic-moduli," J. Phys. (France) **48**, 2139–2151 (1987).
80. Y. K. Park, C. A. Best, K. Badizadegan, R. R. Dasari, M. S. Feld, T. Kuriabova, M. L. Henle, A. J. Levine, and G. Popescu, "Measurement of red blood cell mechanics during morphological changes," Proc. Natl. Acad. Sci. USA **107**, 6731–6736 (2010).
81. C. A. Best, J. E. Cluette-Brown, M. Teruya, A. Teruya, and M. Laposata, "Red blood cell fatty acid ethyl esters: a significant component of fatty acid ethyl esters in the blood," J. Lipid Res. **44**, 612–620 (2003).
82. H. W. G. Lim, M. Wortis, and R. Mukhopadhyay, "Stomatocyte-discocyte-echinocyte sequence of the human red blood cell: evidence for the bilayer-couple hypothesis from membrane mechanics," Proc. Natl. Acad. Sci. USA **99**, 16766–16769 (2002).
83. T. Kuriabova and A. J. Levine, "Nanorheology of viscoelastic shells: applications to viral capsids," Phys. Rev. E **77**, 031921 (2008).
84. P. M. Chaikin and T. C. Lubensky, *Principles of Condensed Matter Physics* (Cambridge University, 1995).
85. Wikipedia, "Malaria," http://en.wikipedia.org/wiki/Main_Page.

86. S. Suresh, J. Spatz, J. P. Mills, A. Micoulet, M. Dao, C. T. Lim, M. Beil, and T. Seufferlein, "Connections between single-cell biomechanics and human disease states: gastrointestinal cancer and malaria," Acta Biomater. **1**, 15–30 (2005).
87. A. Kilejian, "Characterization of a protein correlated with the production of knob-like protrusions on membranes of erythrocytes infected with *Plasmodium falciparum*," Proc. Natl. Acad. Sci. USA **76**, 4650–4653 (1979).
88. I. W. Sherman, "Biochemistry of plasmodium (malarial parasites)," Microbiol. Rev. **43**, 453–495 (1979).
89. D. E. Goldberg, A. F. G. Slater, A. Cerami, and G. B. Henderson, "Hemoglobin degradation in the malaria parasite *Plasmodium falciparum*: an ordered process in a unique organelle," Proc. Natl. Acad. Sci. USA **87**, 2931–2935 (1990).
90. G. B. Nash, E. O'Brien, E. C. Gordon-Smith, and J. A. Dormandy, "Abnormalities in the mechanical properties of red blood cells caused by *Plasmodium falciparum*," Blood **74**, 855–861 (1989).
91. H. A. Cranston, C. W. Boylan, G. L. Carroll, S. P. Sutera, I. Y. Gluzman, and D. J. Krogstad, "*Plasmodium falciparum* maturation abolishes physiologic red cell deformability," Science **223**, 400–403 (1984).
92. M. Paulitschke and G. B. Nash, "Membrane rigidity of red blood cells parasitized by different strains of *Plasmodium falciparum*," J. Lab. Clin. Med. **122**, 581–589 (1993).
93. L. H. Miller, D. I. Baruch, K. Marsh, and O. K. Doumbo, "The pathogenic basis of malaria," Nature **415**, 673–679 (2002).
94. Y. K. Park, M. Diez-Silva, G. Popescu, G. Lykotrafitis, W. Choi, M. S. Feld, and S. Suresh, "Refractive index maps and membrane dynamics of human red blood cells parasitized by *Plasmodium falciparum*," Proc. Natl. Acad. Sci. USA **105**, 13730 (2008).
95. K. R. Williams, K. Gupta, and M. Wasilik, "Etch rates for micromachining processes—part II," J. Microelectromech. Syst. **12**, 761–778 (2003).
96. C. Edwards, K. Wang, R. Zhou, B. Bhaduri, G. Popescu, and L. L. Goddard, "Digital projection photochemical etching defines gray-scale features," Opt. Express **21**, 13547–13554 (2013).
97. E. Spyratou, I. Asproudis, D. Tsoutsi, C. Bacharis, K. Moutsouris, M. Makropoulou, and A. A. Serafetinides, "UV laser ablation of intraocular lenses: SEM and AFM microscopy examination of the biomaterial surface," Appl. Surf. Sci. **256**, 2539–2545 (2010).
98. S. J. Lim, W. Kim, and S. K. Shin, "Surface-dependent, ligand-mediated photochemical etching of CdSe nanoplatelets," J. Am. Chem. Soc. **134**, 7576–7579 (2012).
99. C. J. Hwang, "Optical properties of N-type GaAs. I. Determination of hole diffusion length from optical absorption and photoluminescence measurements," J. Appl. Phys. **40**, 3731–3739 (1969).
100. M. D. Seaberg, D. E. Adams, B. Zhang, D. F. Gardner, M. M. Murnane, and H. C. Kapteyn, "Ultrahigh 22 nm resolution EUV coherent diffraction imaging using a tabletop 13 nm high harmonic source," Proc. SPIE **8324**, 83240D (2012).
101. B. M. Barnes, Y.-J. Sohn, F. Goasmat, H. Zhou, R. M. Silver, and A. Arceo, "Scatterfield microscopy of 22-nm node patterned defects using visible and DUV light," Proc. SPIE **8324**, 83240F (2012).

102. R. Zhou, C. Edwards, A. Arbabi, G. Popescu, and L. L. Goddard, "Detecting 20 nm wide defects in large area nanopatterns using optical interferometric microscopy," Nano Lett. **13**, 3716–3721 (2013).
103. R. Zhou, G. Popescu, and L. L. Goddard, "22 nm node wafer inspection using diffraction phase microscopy and image post-processing," Proc. SPIE **8681**, 86810G (2013).
104. C. Edwards, B. Bhaduri, T. Nguyen, B. Griffin, H. Pham, T. Kim, G. Popescu, and L. L. Goddard, "Effects of spatial coherence in diffraction phase microscopy," Opt. Express **22**, 5133–5146 (2014).
105. T. Nguyen, C. Edwards, L. L. Goddard, and G. Popescu are preparing a manuscript to be called "Quantitative phase imaging with partially coherent illumination."
106. Z. Wang, L. Millet, M. Mir, H. Ding, S. Unarunotai, J. Rogers, M. U. Gillette, and G. Popescu, "Spatial light interference microscopy (SLIM)," Opt. Express **19**, 1016–1026 (2011).
107. J. W. Goodman, *Introduction to Fourier Optics* (Roberts, 2005).
108. R. Barer, "Refractometry and interferometry of living cells," J. Opt. Soc. Am. **47**, 545–556 (1957).
109. Y. K. Park, C. A. Best, T. Auth, N. S. Gov, S. A. Safran, G. Popescu, S. Suresh, and M. S. Feld, "Metabolic remodeling of the human red blood cell membrane," Proc. Natl. Acad. Sci. USA **107**, 1289–1294 (2010).
110. G. Popescu, Y. Park, R. R. Dasari, K. Badizadegan, and M. S. Feld, "Coherence properties of red blood cell membrane motions," Phys. Rev. E **76**, 031902 (2007).
111. G. Popescu, Y. Park, N. Lue, C. Best-Popescu, L. Deflores, R. R. Dasari, M. S. Feld, and K. Badizadegan, "Optical imaging of cell mass and growth dynamics," Am. J. Physiol. Cell Physiol. **295**, C538–C544 (2008).
112. B. Rappaz, F. Charrière, C. Depeursinge, P. J. Magistretti, and P. Marquet, "Simultaneous cell morphometry and refractive index measurement with dual-wavelength digital holographic microscopy and dye-enhanced dispersion of perfusion medium," Opt. Lett. **33**, 744–746 (2008).
113. B. Rappaz, P. Marquet, E. Cuche, Y. Emery, C. Depeursinge, and P. J. Magistretti, "Measurement of the integral refractive index and dynamic cell morphometry of living cells with digital holographic microscopy," Opt. Express **13**, 9361–9373 (2005).
114. Y. Park, T. Yamauchi, W. Choi, R. Dasari, and M. S. Feld, "Spectroscopic phase microscopy for quantifying hemoglobin concentrations in intact red blood cells," Opt. Lett. **34**, 3668–3670 (2009).
115. D. Fu, W. Choi, Y. J. Sung, Z. Yaqoob, R. R. Dasari, and M. Feld, "Quantitative dispersion microscopy," Biomed. Opt. Express **1**, 347–353 (2010).
116. M. Rinehart, Y. Zhu, and A. Wax, "Quantitative phase spectroscopy," Biomed. Opt. Express **3**, 958–965 (2012).
117. H. Pham, B. Bhaduri, H. F. Ding, and G. Popescu, "Spectroscopic diffraction phase microscopy," Opt. Lett. **37**, 3438–3440 (2012).
118. M. Friebel and M. Meinke, "Model function to calculate the refractive index of native hemoglobin in the wavelength range of 250–1100 nm dependent on concentration," Appl. Opt. **45**, 2838–2842 (2006).
119. D. C. Ghiglia and M. D. Pritt, *Two-Dimensional Phase Unwrapping: Theory, Algorithms, and Software* (Wiley, 1998).
120. D. Kirk and W.-M. Hwu, *Programming Massively Parallel Processors Hands-On with CUDA* (Morgan Kaufmann, 2010).

121. P. A. Karasev, D. P. Campbell, and M. A. Richards, "Obtaining a 35× speedup in 2D phase unwrapping using commodity graphics processors," in *IEEE Radar Conference* (IEEE, 2007), pp. 574–578.
122. P. Mistry, S. Braganza, D. Kaeli, and M. Leeser, "Accelerating phase unwrapping and affine transformations for optical quadrature microscopy using CUDA," presented at the 2nd Workshop on General Purpose Processing on Graphics Processing Units, Washington, D.C., 2009.
123. NVIDIA, "NVIDIA CUFFT Library," http://docs.nvidia.com/cuda/cufft/
124. K. Kaushansky and W. J. Williams, *Williams Hematology* (McGraw-Hill, 2011).
125. D. Psaltis, S. R. Quake, and C. H. Yang, "Developing optofluidic technology through the fusion of microfluidics and optics," Nature **442**, 381–386 (2006).
126. D. Tseng, O. Mudanyali, C. Oztoprak, S. O. Isikman, I. Sencan, O. Yaglidere, and A. Ozcan, "Lensfree microscopy on a cellphone," Lab Chip **10**, 1787–1792 (2010).
127. R. S. Weinstein, A. R. Graham, F. Lian, B. L. Braunhut, G. R. Barker, E. A. Krupinski, and A. K. Bhattacharyya, "Reconciliation of diverse telepathology system designs. Historic issues and implications for emerging markets and new applications," APMIS **120**, 256–275 (2012).
128. H. V. Pham, B. Bhaduri, K. Tangella, C. Best-Popescu, and G. Popescu, "Real time blood testing using quantitative phase imaging," PLOS One **8**, e55676 (2013).
129. S. A. Safran, *Statistical Thermodynamics of Surfaces, Interfaces, and Membranes* (Addison-Wesley, 1994).
130. P. B. Canham and A. C. Burton, "Distribution of size and shape in populations of normal human red cells," Circ. Res. **22**, 405–422 (1968).
131. J. Hoshen and R. Kopelman, "Percolation and cluster distribution. I. Cluster multiple labeling technique and critical concentration algorithm," Phys. Rev. B **14**, 3438–3445 (1976).
132. W. K. Pratt, *Digital Image Processing: PIKS Scientific Inside* (Wiley-Interscience, 2007).
133. K. Suzuki, I. Horiba, and N. Sugie, "Linear-time connected-component labeling based on sequential local operations," Comput. Vis. Image Underst. **89**, 1–23 (2003).
134. K. A. Hawick, A. Leist, and D. P. Playne, "Parallel graph component labelling with GPUs and CUDA," Parallel Comput. **36**, 655–678 (2010).
135. O. Kalentev, A. Rai, S. Kemnitz, and R. Schneider, "Connected component labeling on a 2D grid using CUDA," J. Parallel Distrib. Comput. **71**, 615–620 (2011).

Dr. Basanta Bhaduri is a postdoctoral research associate at the Beckman Institute, University of Illinois at Urbana-Champaign (UIUC). He has received the B.Tech. and M.Tech. in Optics and Opto-electronics from Calcutta University, India. He also received the B.Sc. in Physics from Calcutta University. Dr. Bhaduri obtained his Ph.D. in Physics (Applied Optics) in 2007 from the Indian Institute of Technology Madras, India. His research interests are microscopy, optical imaging, image processing, nanotechnology, optical metrology, etc. He was a postdoctoral research fellow in the Department of Mechanical

and Aerospace Engineering, Monash University, Australia for one year and in the Department of Mechanical Engineering, National University of Singapore for two years. Before joining UIUC in June, 2011, he was working as an Assistant Professor in the Department of Physics, Indian Institute of Space Science and Technology (IIST), Trivandrum, India. He is a full member of Sigma Xi and reviewer of several journals. Dr. Bhaduri has presented his work in over 50 journal publications, various conferences, and technical forums, and has earned international awards for his contributions.

Christopher Edwards received his Bachelor's (2007) and Master's degrees (2009) in both electrical and computer engineering from Bradley University, Peoria, Illinois. His research at Bradley focused mostly on robotics and control theory. He graduated at the top of his class for both degrees with a perfect GPA and won several awards and scholarships for his work in engineering and mathematics. He is currently pursuing his Ph.D. at the University of Illinois at Urbana-Champaign (UIUC) with an emphasis in quantitative phase imaging and its applications in material science and biology. He has published a variety of peer-reviewed journal papers and conference proceedings. His work on diffraction phase microscopy was recently published in Nature's new *Light: Science & Applications* journal and was featured as a front page banner article on the National Science Foundation's website. He works in the Photonic Systems Laboratory under Professor Lynford Goddard and in close collaboration with the Quantitative Light Imaging Laboratory under Professor Gabriel Popescu. Besides being a teaching assistant, he has mentored three undergraduate students in their senior thesis research projects on photochemical etching, hydrogen-induced lattice expansion of palladium, and building an environmental stabilization chamber for device testing, which resulted in multiple publications with undergraduate coauthors. Mr. Edwards is also an active student member of several professional organizations including AVS, IEEE, IEEE Photonics Society, OSA, and SPIE as well as the Phi Kappa Phi, Phi Theta Kappa, and Eta Kappa Nu honors societies.

Hoa Pham received a B.S. in electronics and telecommunications from Hanoi University of Technology, Vietnam, in 2002. He obtained his M.S. and Ph.D. in electrical engineering from the University of Illinois at Urbana-Champaign (UIUC) in 2008 and 2013, respectively. He is currently a postdoctoral associate in the Department of Medicine and Bioengineering at the University of Pittsburgh.

Renjie Zhou is currently a Ph.D. candidate in the Electrical and Computer Engineering Department at the University of Illinois at Urbana-Champaign (UIUC). His current research interests are optical microscopy, wafer defect metrology, and 3D object optical reconstruction. He is a student member of the Optical Society of America, SPIE, and the IEEE Photonics Society. While studying at UIUC, he received the Beckman Institute Graduate Fellowship,

Sundaram Seshu International Student Fellowship, Yuen T. Lo Outstanding Graduate Research Award, and SPIE Scholarship in Optics & Photonics. He is a reviewer for *Applied Optics* and *Optics Express*.

Tan Nguyen Tan Huu Nguyen received his Bachelor's degree in automation from the Department of Electrical and Electronic Engineering, Hochiminh University of Technology, Vietnam in 2009 (with highest honor) and a Master's degree in signal processing from the Department of Electrical and Computer Engineering (ECE) at the University of Illinois at Urbana-Champaign (UIUC) in 2012. He has formerly worked with Dr. Rohit Bhargava at the Chemical Imaging and Structures Lab on improving the spatial resolution and data acquisition of Fourier transform infrared spectroscopy using computational tools. Currently, he is a Ph.D. candidate in the ECE department, working with Dr. Minh N. Do and Dr. Gabriel Popescu on machine learning for automatic cancer diagnosis, optical modeling, and building novel quantitative phase imaging modalities. His research interests include optics, machine learning, computer-aided diagnosis, and computational imaging. Tan received the Gold Medal from Hochiminh University of Technology in 2009 for graduation with highest honor, and graduate research awards from SORUN KITAGAWA in 2009 and from TOSHIBA in 2009 and 2010.

Dr. Lynford L. Goddard received the B.S. degree (with distinction) in math and physics, the M.S. degree in electrical engineering, and the Ph.D. degree in physics from Stanford University in 1998, 2003, and 2005, respectively. His doctoral research focused on characterization and modeling of 1.5 μm GaInNAsSb/GaAs lasers. At Lawrence Livermore National Laboratory, he conducted postdoctoral research on photonic integrated circuits, sensors, and data processing systems. Dr. Goddard joined the University of Illinois as an Assistant Professor of Electrical and Computer Engineering in 2007. He was promoted to Associate Professor in 2013. His research group focuses on fabricating, characterizing, and modeling photonic sensors, integrated circuits, and instrumentation, as well as developing new processing techniques and testing novel semiconductor materials and devices. Applications include quantitative phase microscopy for semiconductor wafer metrology, hydrogen detection for fuel cells, carbon dioxide detection for reducing post-harvest food loss, and integrated microring Bragg reflectors for narrow linewidth lasers and next generation chip-scale communication systems.Dr. Goddard is an Associate Editor of the *IEEE Photonics Journal* and an Assistant Topical Editor of the *Journal of the Optical Society of America B*. He is the recipient of a Presidential Early Career Award for Scientists and Engineers (PECASE); the nomination was by the Department of Energy in 2008. He was also the recipient of the inaugural AAAS Early Career Award for Public Engagement with Science in 2011. Dr. Goddard is an author or co-author of over 110 publications and five patents.

Dr. Gabriel Popescu is an Associate Professor in Electrical and Computer Engineering, University of Illinois at Urbana-Champaign (UIUC). He directs the Quantitative Light Imaging Laboratory (QLI Lab) at the Beckman Institute for Advanced Science and Technology. The QLI Lab focuses on developing novel optical methods based on light scattering, interferometry, and microscopy, to image cells and tissues quantitatively and with nanoscale sensitivity. These techniques are applied to both basic science (e.g., cell dynamics, cell growth, intracellular transport, membrane fluctuations, tissue optics) and clinical applications (e.g., blood screening, cancer diagnosis). Over the past decade, Dr. Popescu has been working mainly on *quantitative phase imaging*, a very exciting emerging research field on which he published a book in 2011. He received the B.S. and M.S. in Physics from University of Bucharest, in 1995 and 1996, respectively. He obtained his M.S. in Optics in 1999 and the Ph.D. in Optics in 2002 from the School of Optics/CREOL (now the College of Optics and Photonics), University of Central Florida. Dr. Popescu continued his training with the G. R. Harrison Spectroscopy Laboratory at MIT, working as a postdoctoral associate. He joined UIUC in August 2007. Dr. Popescu founded Phi Optics, Inc., a start-up company that commercializes quantitative phase imaging technology. Professor Popescu received the 2009 NSF CAREER Award, was a 2012 Innovation Discovery Finalist selected by the Office of Technology Management Office, UIUC, and was elected as a 2012-2013 Fellow of the Center for Advanced Studies at UIUC. Dr. Popescu is an Associate Editor of *Optics Express* and *Biomedical Optics Express* and an Editorial Board Member for the *Journal of Biomedical Optics*. He is a SPIE Fellow.